Supplementary Material

Protein Expression and Purification

Three potential N-linked glycosylation sites in mouse (*M. musculus*) MDR1A (Asn-83, Asn-87, Asn-90) were previously eliminated by mutation to glutamine through site-directed mutagenesis of the expression plasmid, pHIL-mdr3.5-His_6 (*1-3*). The C-terminal hexahistidine tagged P-glycoprotein was expressed in *P. pastoris* strain GS115 according to the *Pichia* fermentation process guidelines (Invitrogen, Inc.) with the exception that all of the salts in the fermentation basal salts medium were reduced to half the concentration called for in the manual (*4*). 18 L cultures of *P. pastoris* expressing mouse Pgp were inoculated from overnight cultures and grown in a biofermenter (Bioflow 4500, New Brunswick Scientific). Following an overnight glycerol-fed batch phase, induction of Pgp was accomplished by the addition of methanol (3.6 ml per hour per liter of culture volume) overnight in 50% dissolved oxygen. Cells were lysed by a single pass through a cell disrupter (TS-Series, Constant Systems, Inc.) at 40,000 psi. Cell wall and debris was removed by centrifugation (12,000 x g, 20 min, 4 ˚C) and crude plasma membranes were obtained by centrifugation at 38,400 x g for 4 hours at 4 ˚C. Membranes were resuspended in cold buffer (75 mM NaCl, 15% glycerol, 20 mM tris, pH 8.0) and P-glycoprotein solubilization was achieved with 4.5% Triton® X-100 with stirring for 20 minutes at 4 ˚C. Insoluble material was removed by centrifugation at 38,400 x g, 4 ˚C for 45 minutes and 20 mM imidazole was added to the supernatant before binding to metal resin (Ni-NTA Superflow™, Qiagen). Buffer was exchanged by washing the beads with buffer containing 20 mM imidazole, 0.04% sodium cholate (Sigma) and 0.0675% β-DDM. Protein was eluted with buffer containing 300 mM imidazole, concentrated (Centricon® YM-100; Millipore), spun at 95,000 rpm (TLA120.1 rotor) for 90 min at 4˚ C and subjected to gel filtration chromatography (Superdex™ 200; Amersham Biosciences) at a flow rate of 1.2 ml/min at 4 ˚C and assayed for purity by SDS-PAGE. Elution fractions were pooled, concentrated to 10 mg/ml as measured by the Coomassie assay (Pierce).

Crystallization of Pgp

Mouse Pgp crystallized in space group $P2_12_12_1$ (a = 99.0 Å, b = 119.3 Å, c = 381.3 Å, α,β,γ = 90°) using dodecyl-β-D-maltoside (β-DDM) solubilized protein (Crystal 1, Table S1). Native and derivative crystals shared similar unit cell dimensions and space group. Crystals were grown using the sitting drop method at 4º C by combining protein and precipitant at 1:1 (volume:volume). The highest-diffraction quality crystal (Crystal 2) was from a mutant of mouse Pgp, C952A, grown with precipitant solution consisting of 50 mM Tris (pH 7.3 - 7.5) and 16.8-17.6% PEG 350MME (a = 97.5 Å, b = 115.4 Å, c = 378.9 Å, α,β,γ = 90°). The data from this crystal was used for crystallographic refinement to a resolution of 3.8 Å. Crystals appeared after one week and continued to grow to full size in approximately three weeks. Co-crystals of Pgp with QZ59-RRR compounds were only obtained by first pre-incubating 10 mg/ml mouse Pgp protein with 0.5 mM concentration of ligand overnight. The next morning, the sample was concentrated to 30 mg/ml, diluted back to 10 mg/ml with cold buffer (0.04% sodium cholate and 75 mM NaCl) without β-DDM, and QZ59-RRR was added again to maintain 0.5 mM of inhibitor concentration. Crystallization trays were setup with 1:1 (volume:volume) drop ratio using 5 ul drop sizes. The mother liquor was 20-23% PEG400, 50 mM Tris-HCl pH 7.4-7.9, with no additional salt. Crystals grew about the same rate as those of apo Pgp. QZ59-SSS was grown in a similar manner as QZ59-RRR, except that 0.2 mM of compound was incubated with

2 mg/ml protein overnight. The following morning, the concentration of QZ59-SSS was increased to 0.5 mM for a 2.5 hour incubation. We were unable to obtain ordered binding of QZ59-RRR or QZ59-SSS compounds soaking native, pre-formed crystals with even 5 to 10 times the concentration (1-2 mM) of drug for more than 16 hours as indicated by the lack of selenium peaks in the anomalous Fourier using the procedure described below. At concentrations greater than 2 mM, both QZ59 compounds are insoluble in water.

Data Collection and Structure Determination of Pgp

For the apo structure, a suitable heavy atom derivative, (2-hydroxy-5-nitrophenyl)mercury(II) chloride, (CMNP), was produced for Crystal 1 and 2 by pre-incubation of purified mouse Pgp in 1 mM CMNP on ice for 1 hour prior to crystallization using the same conditions for achieving native crystals. Diffraction data (Table S1) were collected on cryo-cooled crystals at the Stanford Synchrotron Radiation Laboratory (SSRL) (BL 11-1 and BL 9-2), the Advance Photon Source (APS) (23-ID-B, and 23-ID-D) and at the Advanced Light Source (ALS) (BL 8.2.2 and BL 8.3.1). Datasets were processed with HKL2000 (*HKL Research, Inc.*).

The structure of apo Pgp was determined by the multiple anomalous dispersion (MAD) technique using Crystal 1 to build an initial model and subsequently using Crystal 2 for refinement to a resolution of 3.8 Å. Protein phasing, solvent flattening, non-crystallographic symmetry averaging, and phase extension was accomplished using the programs PHASES, SOLVE/RESOLVE and CNS v1.2 (*5-9*). The electron density maps revealed two molecules in the asymmetric unit (PGP1 and PGP2). The initial electron density correlation coefficients from the application of NCS averaging between PGP1 and PGP2 (Fig. S7) are summarized in Table S5. The topologies of the Pgp homologs MsbA and Sav1866 (*10, 11*) were useful as a guide in model building. To verify the topology and the polypeptide chain trace, we generated six single site mutants replacing native cysteine residues with alanine showing a loss of a single mercury site per monomer (Fig. S11A-E,G). We also added one cysteine (C1070) to a Cys-less Pgp construct that showed the addition of this site (Fig. S11F). Each of these seven mutant constructs was labeled with CMNP, crystallized, and diffraction data collected at the Mercury L-III peak (Table S2). Isomorphous and anomalous- difference Fourier maps calculated using these data using model phases confirmed the location and identity of each ordered mercury-labeled cysteine (Fig. S11).

The electron density maps for PGP1 and PGP2 (greater than 1σ) corresponding to mouse Pgp residues 33-626 and 684-1271. The N-terminus (residues 1-33) was not visualized and no electron density was present for most of the linker region (residues 627-683), which is likely a flexible region connecting the two halves of Pgp (*12*). Additionally, no anomalous difference Fourier peaks corresponding to mercury were observed for two CMNP-labeled cysteines (Cys638 and Cys669) in the linker for crystals containing all nine native cysteines (Fig. S6), further supporting the conclusion that most of the linker structure is disordered in this crystal form. Interestingly, both full-length Pgp and co-expressed half-molecules of Pgp devoid of the linker region (Δ627-683) share similar drug-stimulated ATPase activity (data not shown) suggesting that an intact linker is not required for drug-coupled ATPase hydrolysis (*13*).

Crystallographic refinement using data from Crystal 2 was accomplished using the maximum likelihood target with amplitudes and phase probability distribution derived from experimental

MAD phases (mlhl; CNS v1.2). The positions of the mercury for each oxidized cysteine in the model were fixed during the refinement as an additional constraint on the model. A final round of group B-factor refinement and bulk solvent correction produced a single model with an R_{cryst} of 30.6% and R_{free} of 34.7% (Table S2). Additional modeling restraints used during crystallographic refinement included hydrogen-bonding constraints for all secondary structure elements and harmonic non-crystallographic restraints (300 kcal/mole) between PGP1 and PGP2 for the TM domains (four groups: residues 33-208 and 322-368; residues 694-851 and 962-1008, residues 210-320, and residues 853-960), and the NBDs (two groups: residues 385-626; residues 1031-1270) of PGP1 and PGP2 corresponding to those in Table S5. This model, without mercury, was also used to generate isomorphous difference and anomalous Fourier maps revealing the position and identity of ordered cysteines in the structure (Table S2, Fig. S7C, S11).

The x-ray co-crystal structures with QZ59-RRR and QZ59-SSS, variants of dendroamide A (*14*), were solved by the molecular replacement method using Pgp models from the apo crystal form. Because of the nearly isomorphous unit cell dimensions with apo (Table S1), rigid body refinement (CNS v1.2) could be conveniently used. Crystallographic refinement was accomplished using a maximum likelihood target function using amplitudes only (mlf; CNS v1.2) and harmonic constraints on the coordinates (40 kcal/mole). Restraints for hydrogen bonding and non-crystallographic symmetry were the same as those used for the apo structure refinement. The orientation of each QZ59 molecule was determined using Fo-Fc difference density using model phases without the ligand. The positions of the ligands were also confirmed by using peaks from the anomalous Fourier using data collected on the Se K edge (Fig. S15; Table S1). In the case of QZ59-SSS co-crystal structure, a selenium position for the ligand in the "upper" site did not have a peak in either PGP1 or PGP2. We presume, based on the absence of Fo-Fc difference density for the ligand, that a portion of the QZ59-SSS molecule closer to the extracellular side has a degree of disorder and is likely caused by the hydrophobic and flexible residues near the ligand. Unlike the "lower" site, which has polar interactions, the region near the "upper" site contains hydrophobic aromatic (Tyr113, Tyr949, Phe953, and Phe71) and three non-polar methionine (Met67, Met68, and Met74) residues. As a consequence, we only include the part of the ligand in the "upper site" that has strong Fo-Fc density in PGP1 and PGP2.

All structures of Pgp were verified using a sigmaa weighted 2Fo-Fc composite simulated annealing (SA) omit map (iteratively omitting 5% of the model) as well as multiple Fo-Fc SA difference maps (Figs. S8-S10, S15-S17). The Fo-Fc maps were calculated using CNS v1.2 systematically omitting eleven consecutive residues throughout the model generously omitting a neighboring sphere size of 4.0 Å and a map cushion surrounding the omitted region of 2.0 Å (Fig. S8-S10, S15D-E, S16, S17). For the QZ59-RRR and QZ59-SSS structures, the difference density was generated by omitting each ligand individually from the model. The Fo-Fc maps could be conveniently viewed as a single composite map for confirming the residue and ligand positions.

Model Building and Figures
All models were built using the programs CHAIN (*15*), Coot (*16*), and PyMOL (*17*). Figures were generated using PyMOL and Adobe Photoshop 7.0.

Chemical Synthesis of QZ59 compounds
N-Boc-(*S*)-Val-Selenamide (Fig. S21-1) was prepared from *N*-Boc-(*S*)-Val-OH according to the literature procedures (*18, 19*). A mixture of **1** (500 mg, 1.8 mmol), ethylbromopyruvate (0.25mL, 90% purity, 2.0 mmol) and pyridine (1.5 mL, 18 mmol) in ethanol (40 mL) was refluxed under N_2 for 12 hrs. The solvent was evaporated and the residue was submitted to purification by silica gel chromatography (ethyl acetate:hexane = 1:5). *N*-Boc-*rac*-Val-selenazole-OEt (Fig. S21-2) was obtained as a white powder (609 mg, 90.4%), whereas the sole stereocenter in **2** was completely racemized during the cyclization, confirmed by zero optical rotation value and by the resolution of two peaks with identical peak areas using chiral HPLC technique (Chiralpak AD column, hexane/isopropanol = 1:9). ^{1}H NMR (500 MHz, $CDCl_3$) δ 0.91 (d, *J* = 9.0 Hz, 3H), 1.01 (d, *J* = 9.0 Hz, 3H), 1.37 (t, *J* = 9.0 Hz, 3H), 1.45 (s, 9H), 2.51-2.52 (m, 1H), 4.40 (q, *J* = 8.5 Hz, 2H), 4.85 (m, 1H), 5.26-5.28 (m, 1H), 8.80 (s, 1H); ^{13}C NMR (125 MHz, $CDCl_3$) δ 14.7, 17.4, 20.0, 28.7, 33.3, 61.0, 61.7, 80.6, 134.5, 148.8, 155.8, 162.0, 181.4.

The ethyl ester of *N*-Boc-*rac*-Val-selenazole-OEt (**2**) (700 mg, 1.87 mmol) was hydrolyzed in the solution of NaOH (680 mg, 17 mmol) in mixed solvents (THF-MeOH-H_2O = 10:2:3), and the *N*-Boc protective group was subsequently removed by reaction with trifluoacetic acid (12.6 mL) in dichloromethane (38 mL). After removal of the solvent, the amino acid (Fig. S21-3) was directly dissolved in anhydrous acetonitrile (20 mL). Diisopropylethylamine (DIEPA) (1.23 mL, 7.48 mmol) and pentafluorophenol diphenylphosphinate (FDPP) (1.44 g, 3.74 mmol) were added to the above solution at room temperature under N_2. The reaction was monitored by TLC. Upon completion of the reaction, the solvent was removed in vacuo and the residue was partitioned between CH_2Cl_2 (45 mL) and H_2O (30 mL). The organic phase was washed successively with aq. HCl (2 M, 50 mL), aq. NaOH (1 M, 2x50 mL), H_2O (50 mL) and brine (50 mL), dried over $MgSO_4$ and filtered. The solvent was then removed in vacuo, and the residue was purified by silica gel chromatography to give an inseparable mixture of cyclic hexpeptides as the major products (211 mg, 49.3%).

The mixture of the cyclic hexapeptides, comprised of a maximal four stereoisomers (QZ59-RRR, QZ59-SSS, QZ59-RRS and QZ59-SSR), was separated successively by reverse phase HPLC (C18 column, CH_3CN/H_2O = 5:2) and chiral HPLC (Chiralcel OD-H or Chiralpak IB column, isopropanol/hexane = 1:3) (Fig. S21). Reverse phase HPLC was used to separate the two pairs of enantiomers, and chiral HPLC was to separate each pair of enantiomers to give the optically pure components. The relative configuration of each stereoisomer was assigned on the basis of their symmetry as determined by ^{1}H NMR spectroscopy. In order to unambiguously assign the absolute configuration of QZ59-RRR and QZ59-SSS, we also synthesized the optically pure sulfur compounds (cyclic-tris-(*R*)-valinethiazole and cylic-tris-(*S*)-valinethiazole) from known procedures (*20*). The absolute stereochemistry of QZ59-RRR and QZ59-SSS was assigned by comparing the sign of the optical rotation and the elution order on chiral HPLC column with the respective thiazole compounds (Table S4). Data for QZ59-RRS and QZ59-SSR were not shown.

QZ59-SSS: ^{1}H NMR (500 MHz, $CDCl_3$, 25 °C, TMS) δ 1.07 (d, *J* = 7.0 Hz, 9H), 1.09 (d, *J* = 7.5 Hz, 9H), 2.24-2.31 (m, 3H), 5.52 (dd, *J* = 5.5, 9.5 Hz, 3H), 8.37 (d, *J* = 9.5 Hz, 3H), 8.81 (s, 3H); ^{13}C NMR (125 MHz, $CDCl_3$) δ 18.6, 19.4, 35.4, 58.2, 131.1, 150.3, 160.5, 175.6; HRMS (ESI) calcd for $C_{24}H_{31}N_6Se_3O_3$ $(M+H)^+$ 690.9948, found 690.9959.
QZ59-RRR: The ^{1}H and ^{13}C NMR spectra of QZ59-RRR are identical to those of QZ59-SSS.

ATPase Activity
ATPase activity of detergent-solubilized Pgp was assayed in the presence of 0.1 mg/ml 1-palmitoyl-2-oleoyl-sn-glycero-3-phosphoethanolamine (POPE) lipid (Avanti) that was included at all steps during the purification (*21*). To test ATPase activity of Pgp recovered from crystals, crystals were transferred into fresh mother liquor twice to remove non-crystallized Pgp. Crystals were dissolved in 0.065% w/v β-DDM containing 0.1 mg/ml brain total lipids (Avanti) and washed with three steps of concentration-dilution before ATPase assay. Protein concentrations were measured using a Coomassie assay. ATPase activity was measured using an ATP-regenerating system described by Vogel and Steinhart (*22*) and modified by Urbatsch and Senior (*23*). Briefly, 1 μg of mouse Pgp was added to 100 μl of Linked Enzyme (LE) buffer at 37 °C containing 6 mM phosphoenolpyruvate (PEP), 1mM NADH, 10 units of lactate dehydrogenase (LDH), 10 units of pyruvate kinase (PK), 10mM Mg^{2+}ATP and 50mM Tris-HCl, pH 7.5. ATP hydrolysis was measured in parallel samples as the decrease in absorbance of NADH at 340 nm per minute using a DTX880 multiplate spectrofluorimeter (Beckman-Coulter). Control samples contained LE buffer without any added Pgp and were subtracted as background values. Verapamil dependent ATPase activity was determined by adding increasing amounts of verapamil (0-150 μM) to the above LE reaction. Inhibition of ATPase by the QZ59 compounds was determined by adding increasing amounts of the compounds (0-250 μM) to the above LE reaction that was supplemented with 50 μM verapamil. The data were plotted as mean values with standard deviation and fit using nonlinear regression in the GraphPad Prism or Sigmaplot software packages with the equations: $Y=V_{max}*X/(K_m+X)$ for Fig. S2A and $Y=V_o-((V_o-V_{fin})-X^b/(K_i^b+X^b))$ for QZ59-SSS in Fig. S2B and $Y=V_{fin}+((V_o-V_{fin})+((V_{max}-V_o)*X/(K_m+X)))*(1-(X/(K_i+X)))$ for QZ59-RRR in Fig. S2B, where V_o is the verapamil-stimulated activity in the absence of inhibitor, V_{fin} is the activity at infinitive concentrations of inhibitor, V_{max} is the maximum activity, K_m is the concentration for half-maximal stimulation, K_i is the concentration for half-maximal inhibition (IC_{50}), b is the Hill coefficient, and X the concentration of inhibitor. Each data point was the average of three to four independent observations minus the background decrease in absorbance.

Calcein-AM transport assay
Chinese hamster ovary cells CR1R12 were previously selected in colchicine and overexpressed high levels of Pgp accounting for ~20% of the total plasma membrane protein (*24*). CR1R12 and their parental control cells AuxB1 were cultured as described (*24*). For transport assays, $5x10^5$ CR1R12 cells were pre-incubated with increasing concentrations of the inhibitors for 15 min at RT in 100 μl of culture medium. Calcein-AM (0.25 μM) was added and the fluorescence intensity (excitation 494 nm, emission 517 nm) monitored after 30 min incubation at RT in a FluoroLog-3 fluorimeter (*Jobin Yvon Horiba*) equipped with a 96-well plate reader. 100% was the maximum fluorescence seen upon full inhibition of Pgp in CR1R12 cells and was 35,000 ± 5,000 (arbitrary units). The compounds had no effect on calcein-AM accumulation in the

parental AuxB1 control cells for which the relative fluorescence intensities remained constant at 35,000 ± 5,000 (100%) over the entire concentration range assayed (data not shown).

Growth inhibition of CR1R12 cells by colchicine and their sensitization by QZ59 compounds

CR1R12 cells were grown in the presence of increasing concentrations of the anti-cancer drug colchicine for four days at 37^{o}C, 5% CO_2 and then the cell density determined using sulforhodamine (*25*). 100% is the growth in the absence of colchicine. QZ59 compounds were added to the growth media at the concentrations indicated from stocks in DMSO with the final DMSO concentration not exceeding 1%. Parental AuxB1 cells expressing very low amounts of Pgp were included as controls.

Fig. S1

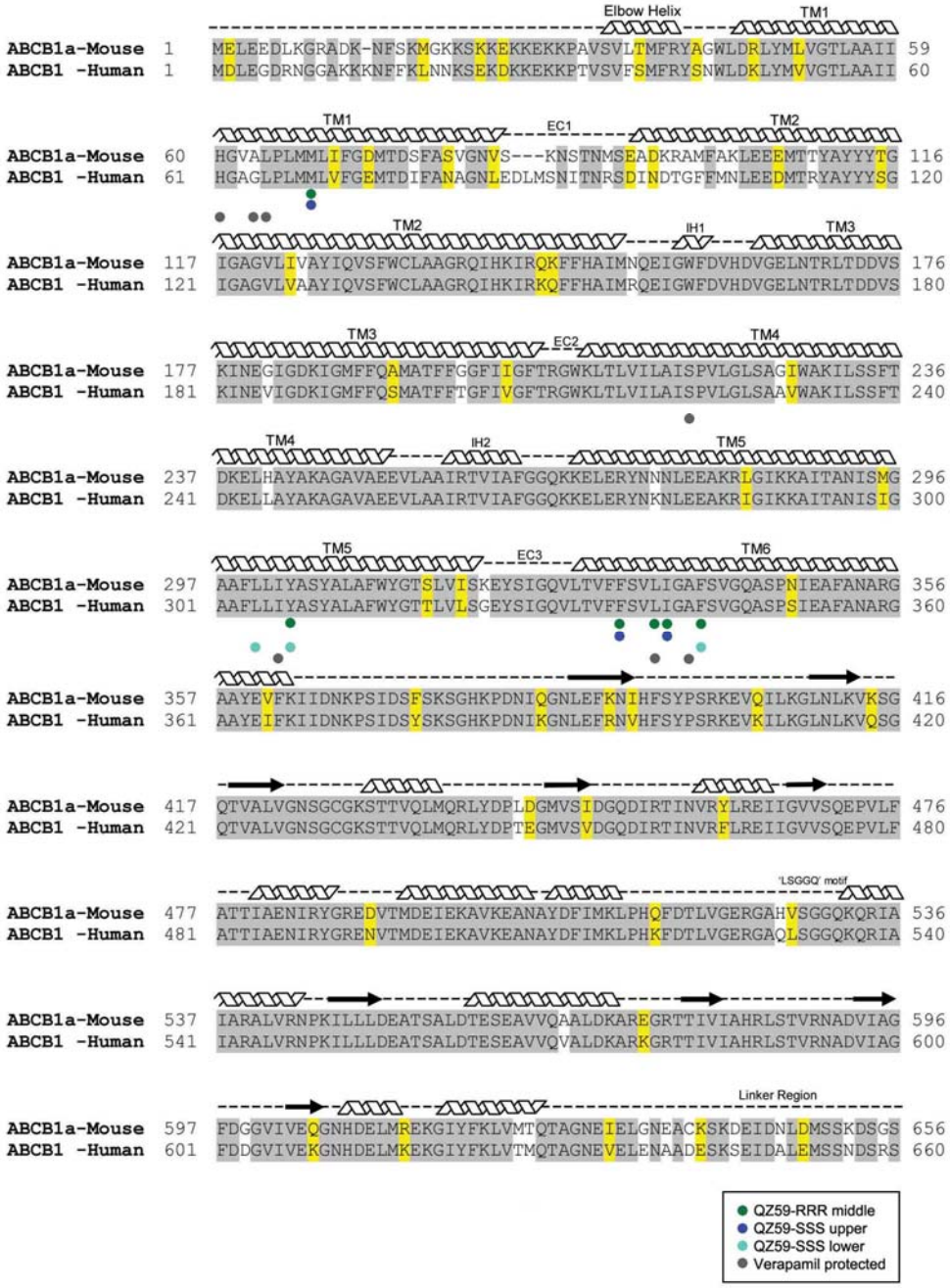
Elbow Helix
TM1
ABCB1a-Mouse 1 MELEEDLKGRADK-NFSKMGKKSKKEKKEKKPAVSVLTMFRYAGWLDRLYMLVGTLAAII 59
ABCB1 -Human 1 MDLEGDRNGGAKKKNFFKLNNKSEKDKKEKKPTVSVFSMFRYSNWLDKLYMVVGTLAAII 60
TM1
EC1
TM2
ABCB1a-Mouse 60 HGVALPLMMLIFGDMTDSFASVGNVS---KNSTNMSEADKRAMFAKLEEEMTTYAYYYTG 116
ABCB1 -Human 61 HGAGLPLMMLVFGEMTDIFANAGNLEDLMSNITNRSDINDTGFFMNLEEDMTRYAYYYSG 120
TM2
IH1
TM3
ABCB1a-Mouse 117 IGAGVLIVAYIQVSFWCLAAGRQIHKIRQKFFHAIMNQEIGWFDVHDVGELNTRLTDDVS 176
ABCB1 -Human 121 IGAGVLVAAYIQVSFWCLAAGRQIHKIRKQFFHAIMRQEIGWFDVHDVGELNTRLTDDVS 180
TM3
EC2
TM4
ABCB1a-Mouse 177 KINEGIGDKIGMFFQAMATFFGGFIIGFTRGWKLTLVILAISPVLGLSAGIWAKILSSFT 236
ABCB1 -Human 181 KINEVIGDKIGMFFQSMATFFTGFIVGFTRGWKLTLVILAISPVLGLSAAVWAKILSSFT 240
TM4
IH2
TM5
ABCB1a-Mouse 237 DKELHAYAKAGAVAEEVLAAIRTVIAFGGQKKELERYNNNLEEAKRLGIKKAITANISMG 296
ABCB1 -Human 241 DKELLAYAKAGAVAEEVLAAIRTVIAFGGQKKELERYNKNLEEAKRIGIKKAITANISIG 300
TM5
EC3
TM6
ABCB1a-Mouse 297 AAFLLIYASYALAFWYGTSLVISKEYSIGQVLTVFFSVLIGAFSVGQASPNIEAFANARG 356
ABCB1 -Human 301 AAFLLIYASYALAFWYGTTLVLSGEYSIGQVLTVFFSVLIGAFSVGQASPSIEAFANARG 360
ABCB1a-Mouse 357 AAYEVFKIIDNKPSIDSFSKSGHKPDNIQGNLEFKNIHFSYPSRKEVQILKGLNLKVKSG 416
ABCB1 -Human 361 AAYEIFKIIDNKPSIDSYSKSGHKPDNIKGNLEFRNVHFSYPSRKEVKILKGLNLKVQSG 420
ABCB1a-Mouse 417 QTVALVGNSGCGKSTTVQLMQRLYDPLDGMVSIDGQDIRTINVRYLREIIGVVSQEPVLF 476
ABCB1 -Human 421 QTVALVGNSGCGKSTTVQLMQRLYDPTEGMVSVDGQDIRTINVRFLREIIGVVSQEPVLF 480
'LSGGQ' motif
ABCB1a-Mouse 477 ATTIAENIRYGREDVTMDEIEKAVKEANAYDFIMKLPHQFDTLVGERGAHVSGGQKQRIA 536
ABCB1 -Human 481 ATTIAENIRYGRENVTMDEIEKAVKEANAYDFIMKLPHKFDTLVGERGAQLSGGQKQRIA 540
ABCB1a-Mouse 537 IARALVRNPKILLLDEATSALDTESEAVVQAALDKAREGRTTIVIAHRLSTVRNADVIAG 596
ABCB1 -Human 541 IARALVRNPKILLLDEATSALDTESEAVVQVALDKARKGRTTIVIAHRLSTVRNADVIAG 600
Linker Region
ABCB1a-Mouse 597 FDGGVIVEQGNHDELMREKGIYFKLVMTQTAGNEIELGNEACKSKDEIDNLDMSSKDSGS 656
ABCB1 -Human 601 FDDGVIVEKGNHDELMKEKGIYFKLVTMQTAGNEVELENAADESKSEIDALEMSSNDSRS 660
QZ59-RRR middle
QZ59-SSS upper
QZ59-SSS lower
Verapamil protected

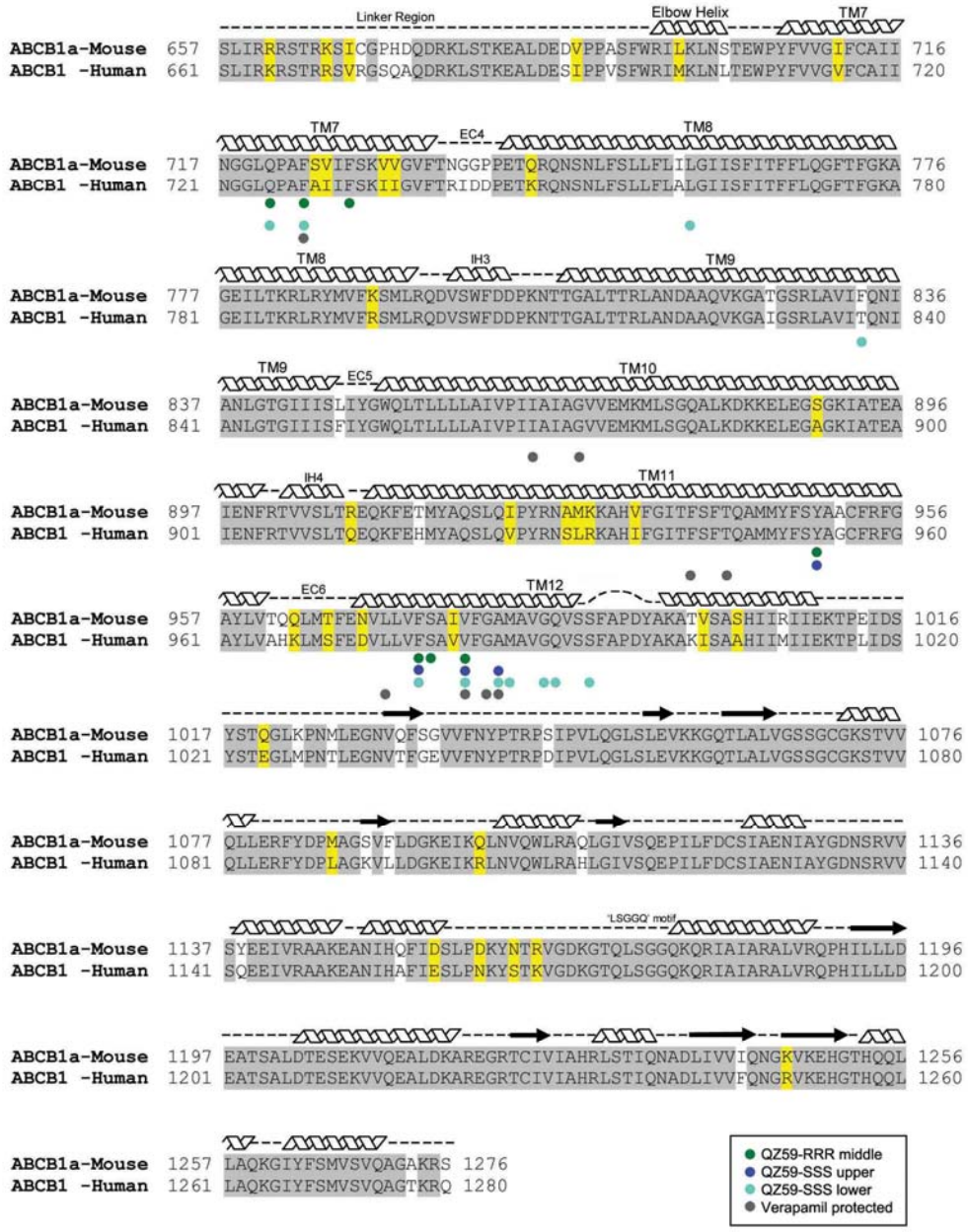

Fig. S1. Amino acid sequence alignment of mouse and human Pgp. Residues interacting with QZ59-RRR in the "middle" site (●), and QZ59-SSS "upper" (●) and "lower" (●) sites are indicated. All residues that are protected from MTS-verapamil labeling by verapamil (●) in previous studies (*26-30*) are also shown. Secondary structure for Pgp is shown above the protein sequence alignment.

Fig. S2

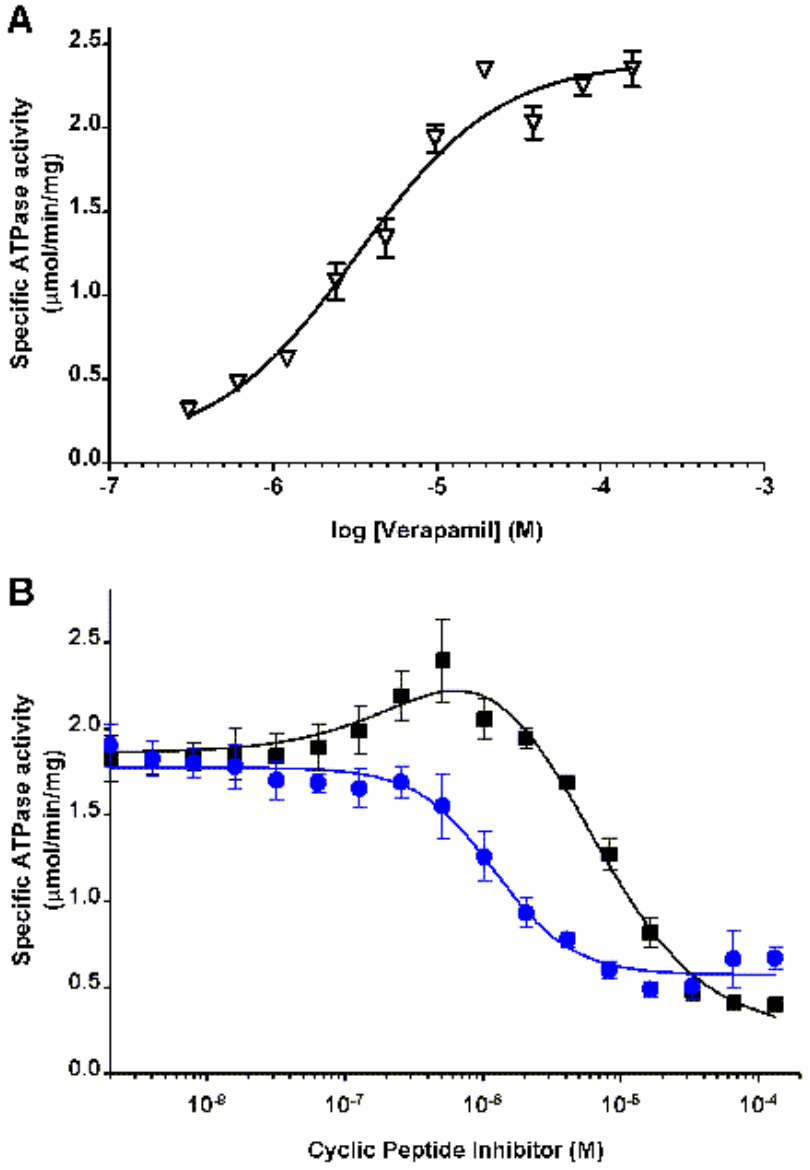

Fig. S2. ATPase activity of Pgp. (A) Verapamil concentration dependent ATPase activity of purified Pgp. The concentration required for half-maximal stimulation was 2.9 μM ± 0.33. (B) Concentration-dependent inhibition of verapamil stimulated (50 μM) ATPase activity by QZ59-RRR (■) and QZ59-SSS (●). Both inhibitors restore PGP to basal activity level (~0.3 μmol/min/mg) with IC_{50} values of 4.8 ± 2.6 and 1.2 ± 0.33 μM, respectively. The averages and SD of triplicate experiments are shown and solid lines are fits to the Hill equation.

Fig. S3

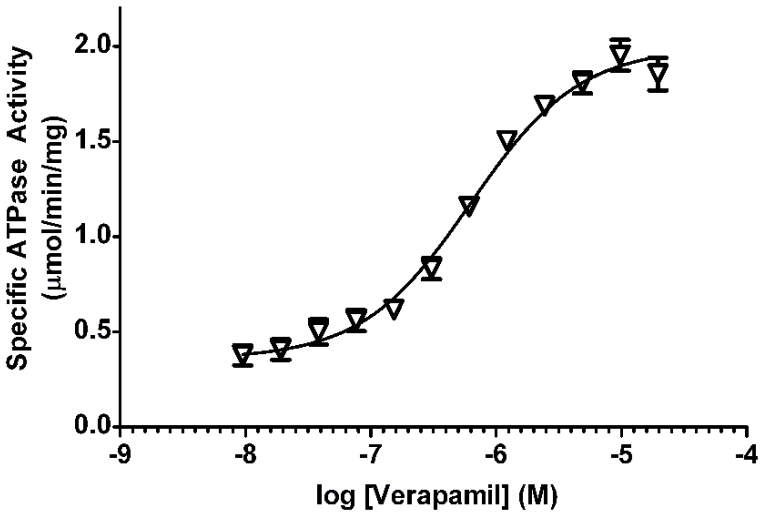

Fig. S3. Functional Pgp protein recovered from crystals. Verapamil concentration dependent ATPase activity of Pgp recovered from crystals after reactivation in the presence of phospholipid and the reducing agent TCEP. The concentration required for half-maximal stimulation by verapamil was 0.28 μM. The averages and SD of triplicate experiments are shown and the solid line is a fit to the Hill equation.

Fig. S4

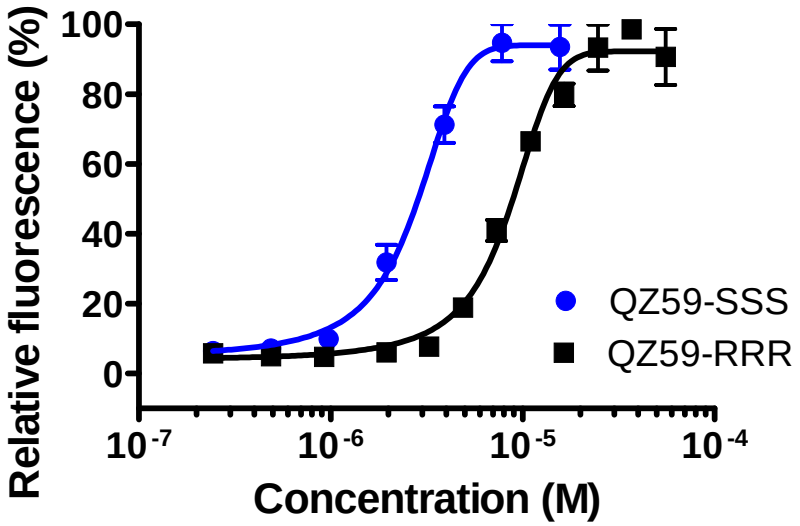

Fig. S4. Inhibition of Pgp-mediated calcein-AM transport by QZ59 compounds. Both QZ59-SSS (●) and QZ59-RRR (■) restored calcein-AM uptake in Pgp-overexpressing CR1R12 cells (*24*) with IC_{50} values of 1.2 ± 0.33 μM and 4.8 ± 2.6 μM. Known Pgp inhibitors cyclosporin A and verapamil have IC_{50} values of 3 and 13 μM measured in the same assay. The averages and SD of duplicate experiments are shown and solid lines are fits to the Hill equation.

Fig. S5

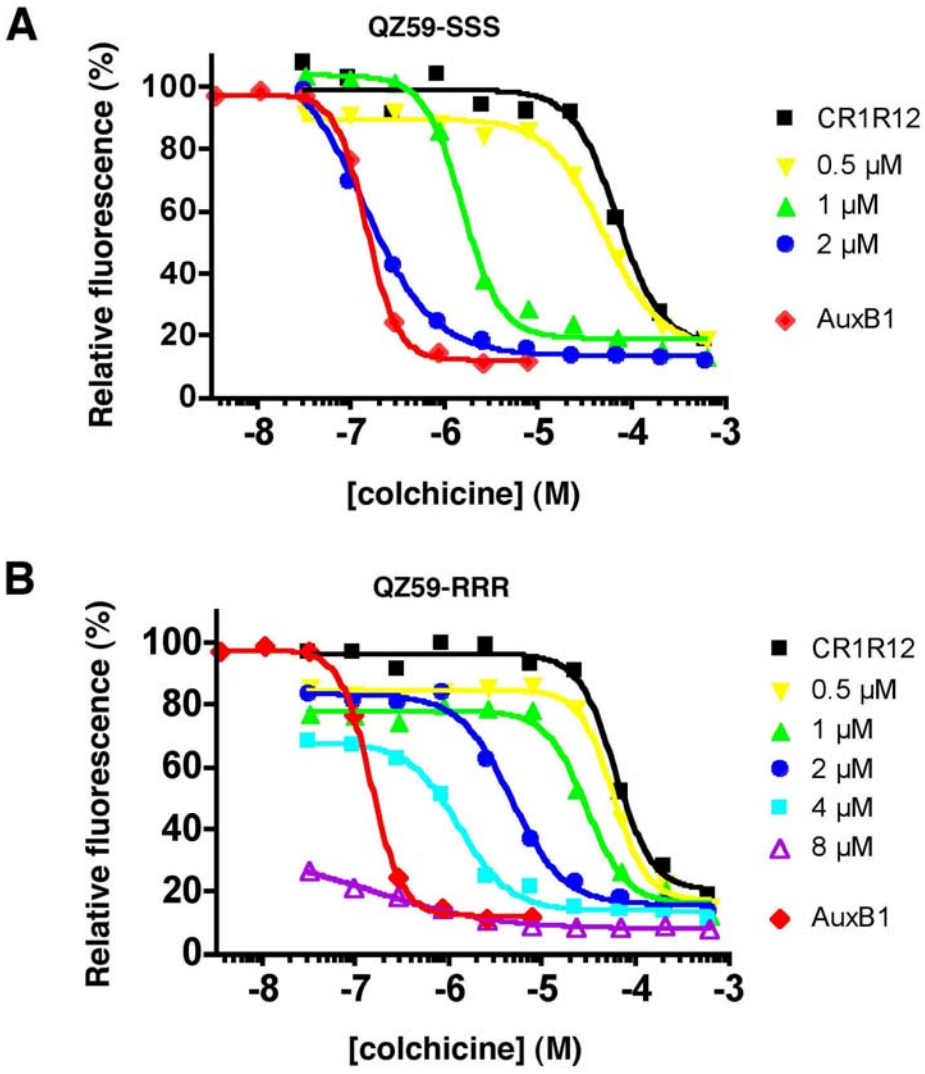

Fig. S5. Sensitization of CR1R12 cells to the anti-cancer drug colchicine by QZ59 compounds. Pgp-overexpressing CR1R12 cells (■) are ~500 times more resistant to the anticancer drug colchicine than their parental control cells AuxB1 (◆) with 50% growth inhibition (GI_{50}) seen at 65 μM and 0.15 μM, respectively. (A) Presence of QZ59-SSS in the growth media sensitized the CR1R12 cells to colchicine in a concentration-dependent manner with full reversal of Pgp-mediated MDR seen at 2 μM (●); this concentration gave essentially the same GI_{50} value (0.16 μM) as seen in AuxB1 cells. (B) Presence of increasing concentrations of QZ59-RRR (▼, ▲, ●, and ■) also sensitized CR1R12 cells to colchicine, where full reversal of MDR was not observed because this compound became cytotoxic at higher concentrations (△). The data emphasize the potential of QZ59-SSS for reversing MDR *in-vivo* and its stereo-selective interactions with the Pgp pump. Representatives of two independent experiments are shown.

Fig. S6

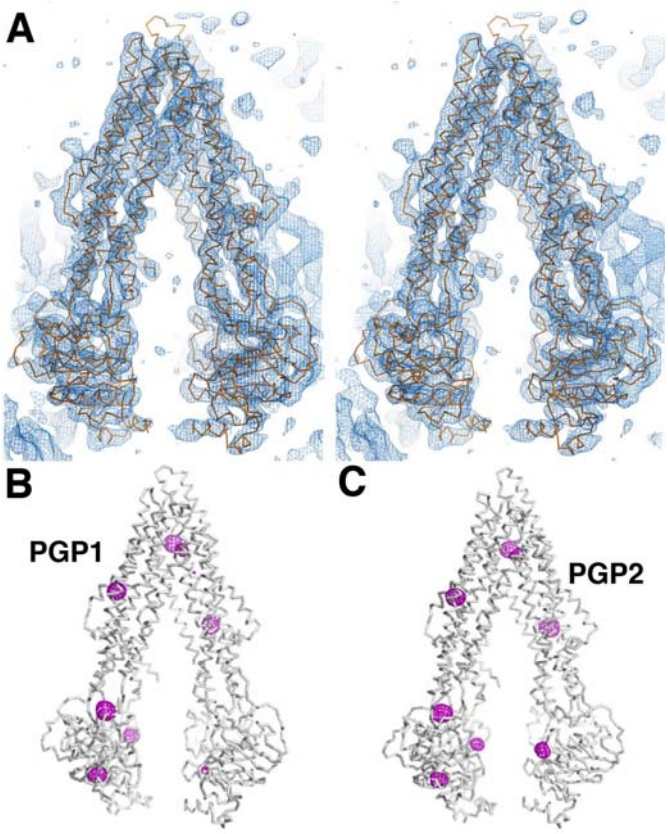

D

Anomalous peak	Height (σ)	Model position
Peak 1	22.5	C133 (PGP2)
Peak 2	21.4	C713 (PGP1)
Peak 3	20.2	C952 (PGP1)
Peak 4	20.1	C1121 (PGP2)
Peak 5	20.1	C713 (PGP2)
Peak 6	19.8	C1121 (PGP1)
Peak 7	19.2	C952 (PGP2)
Peak 8	17.3	C133 (PGP1)
Peak 9	15.0	C1223 (PGP1)
Peak 10	13.5	C1223 (PGP2)
Peak 11	13.3	C1070 (PGP1)
Peak 12	9.3	F71 (PGP2)
Peak 13	9.2	F71 (PGP1)
Peak 14	9.2	C1070 (PGP2)
Peak 15	6.8	C427 (PGP2)
Peak 16	5.4	C427 (PGP1)
Peak 17	4.7	micellar space

Fig. S6. Electron density and topology of Pgp Crystal 1. (A) Stereo view of experimental electron density contoured at 1σ. (B and C) Anomalous Fourier map (magenta) contoured at 4σ showing peaks corresponding to CMNP-labeled Pgp having all nine native cysteines (Crystal 1) at 4.5 Å resolution for (B) PGP1 and (C) PGP2 in the asymmetric unit. Strong peaks corresponding to each of the seven ordered cysteines per monomer can be clearly seen. Peaks corresponding to the two linker-region cysteines are absent implicating a disordered linker region. (D) Table of peak heights from the anomalous Fourier map of Crystal 1 and their associated positions relative to the model.

Fig. S7

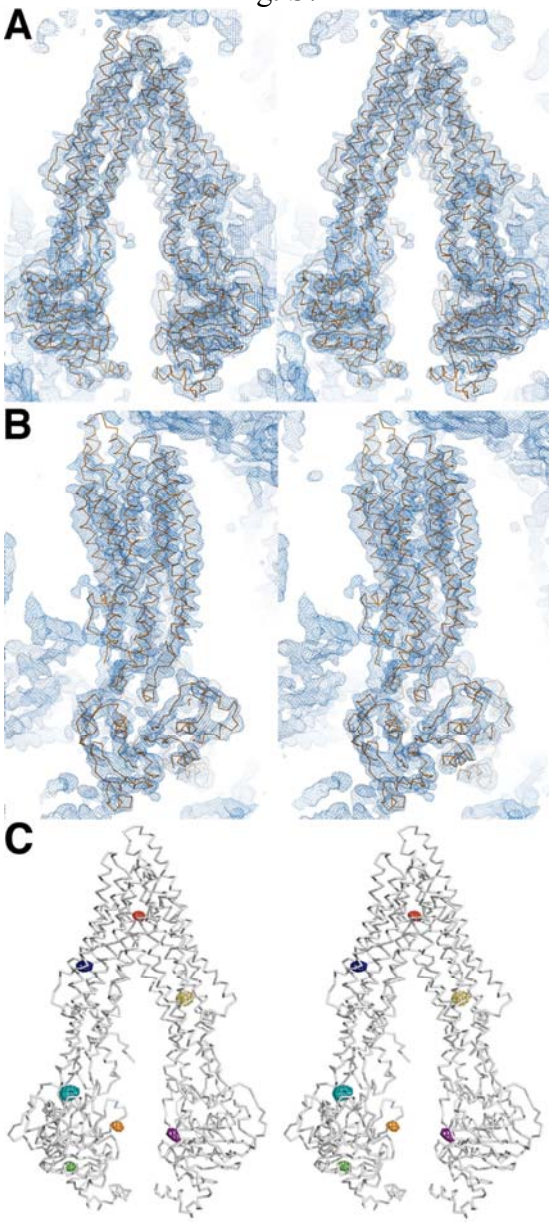

Fig. S7. Electron density and topology of Pgp. (A) Stereo view of electron density (blue mesh) contoured at 1σ derived from MAD experimental phases and NCS averaging from the mercury-labeled C952A dataset at 3.8 Å. The Cα trace of a Pgp monomer is shown in orange. (B) View rotated 90˚ about the pseudo molecular 2-fold axis relating the two halves of the molecule. Additional electron density surrounding this molecule is from symmetry-related copies in the unit cell. (C) Stereo view of the Pgp backbone (grey) with isomorphous and anomalous difference Fourier electron density peaks superimposed. Positive isomorphous difference density peaks validating both the positions and identities of cysteine residues in the model by point mutations were calculated by subtracting the following datasets from the C952A dataset: C133A (yellow), C427A (magenta), C713A (blue), C1121A (cyan), C1223A (green). The peak corresponding to position 952 in the model (red) was achieved by subtracting C952A dataset from C713A. The peak corresponding to position 1070 (orange) is from an anomalous difference Fourier calculation of the A1070C mutant made from a Cysless-Pgp construct. All peaks in (C) are contoured at 7σ with the exception of C427A (4σ) and A1070C (5σ).

Fig. S8

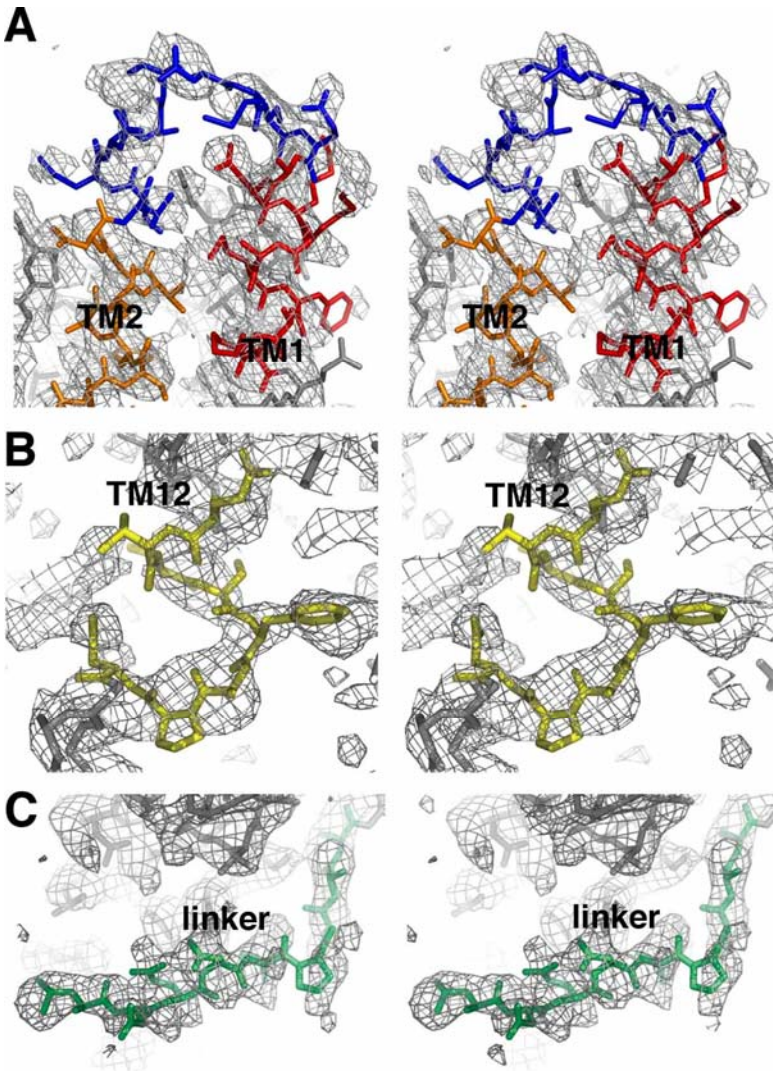

Fig. S8. Fo-Fc density of unique structural features of Pgp. (A) Closeup of first extracellular loop (EC1) containing the N-linked glycosylation sites that were removed for crystallography, (B) close up of a break in the α-helical structure of TM12 (residues 989-994), (C) close-up of the portion of the linker region (residues 684 to 692) that is ordered leading towards the C-terminal half of the molecule shown in green. Fo-Fc density in all three panels is shown in grey. Difference density for an entire Pgp molecule was achieved by superimposing individual Fo-Fc maps calculated using sequential segments of eleven residues that were iteratively omitted from the model calculated with a neighboring sphere size of 4 Å and a map cushion of 2 Å. The maps are contoured at 2σ with a B-factor of -50 $Å^2$ applied to the structure factors (CNS v1.2). In (A), portions of the three windows omitted from the model are shown in three different colors (orange, blue, and red).

Fig. S9

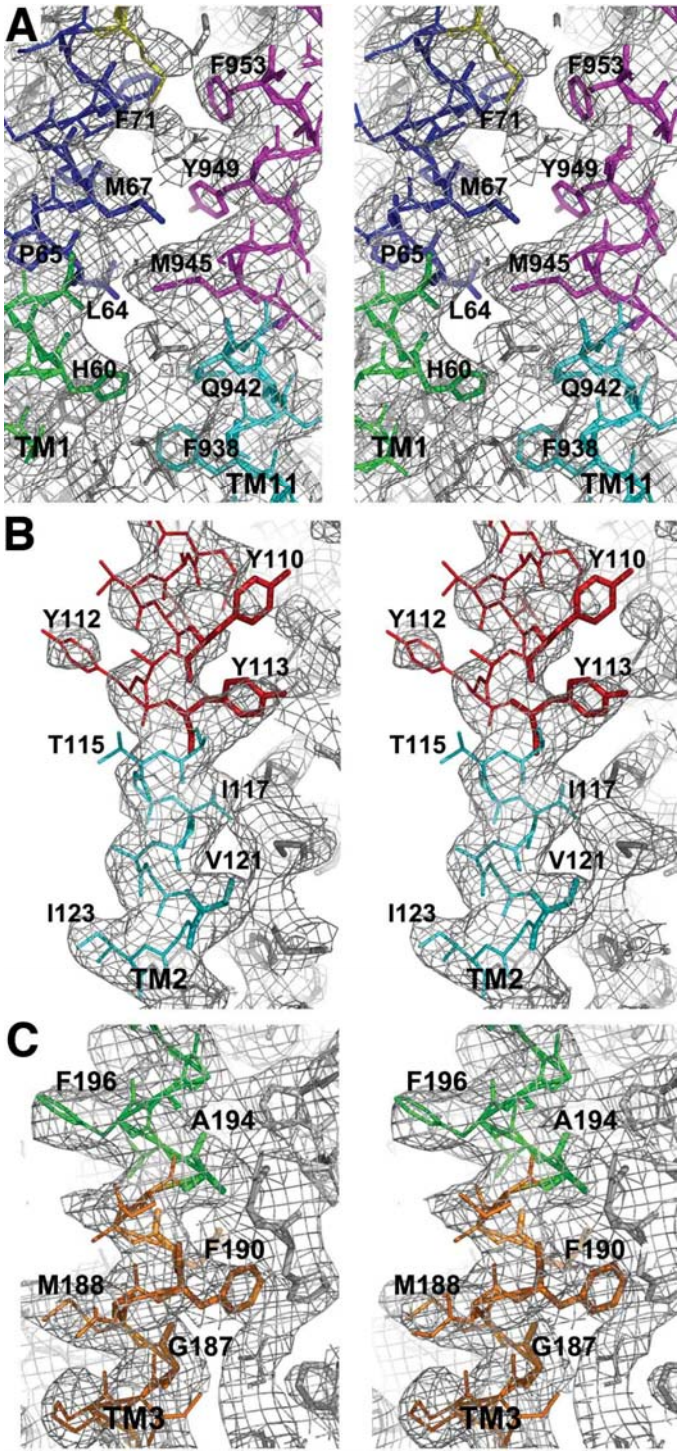
A
F953
F71
Y949
M67
P65
M945
L64
H60
Q942
TM1
F938
TM11
B
Y110
Y112
Y113
T115
I117
V121
I123
TM2
C
F196
A194
F190
M188
G187
TM3

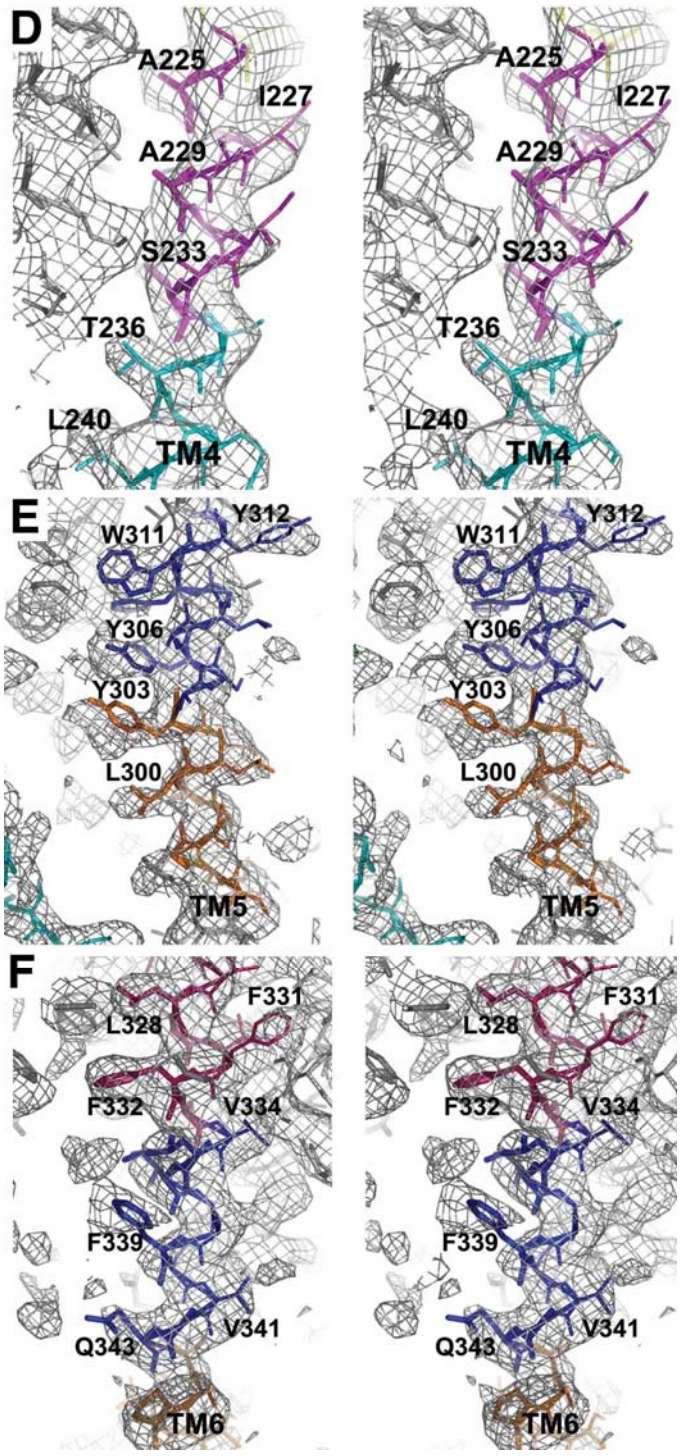
D
A225
I227
A229
S233
T236
L240
TM4
A225
I227
A229
S233
T236
L240
TM4
E
W311
Y312
Y306
Y303
L300
TM5
W311
Y312
Y306
Y303
L300
TM5
F
F331
L328
F332
V334
F339
V341
Q343
TM6
F331
L328
F332
V334
F339
V341
Q343
TM6

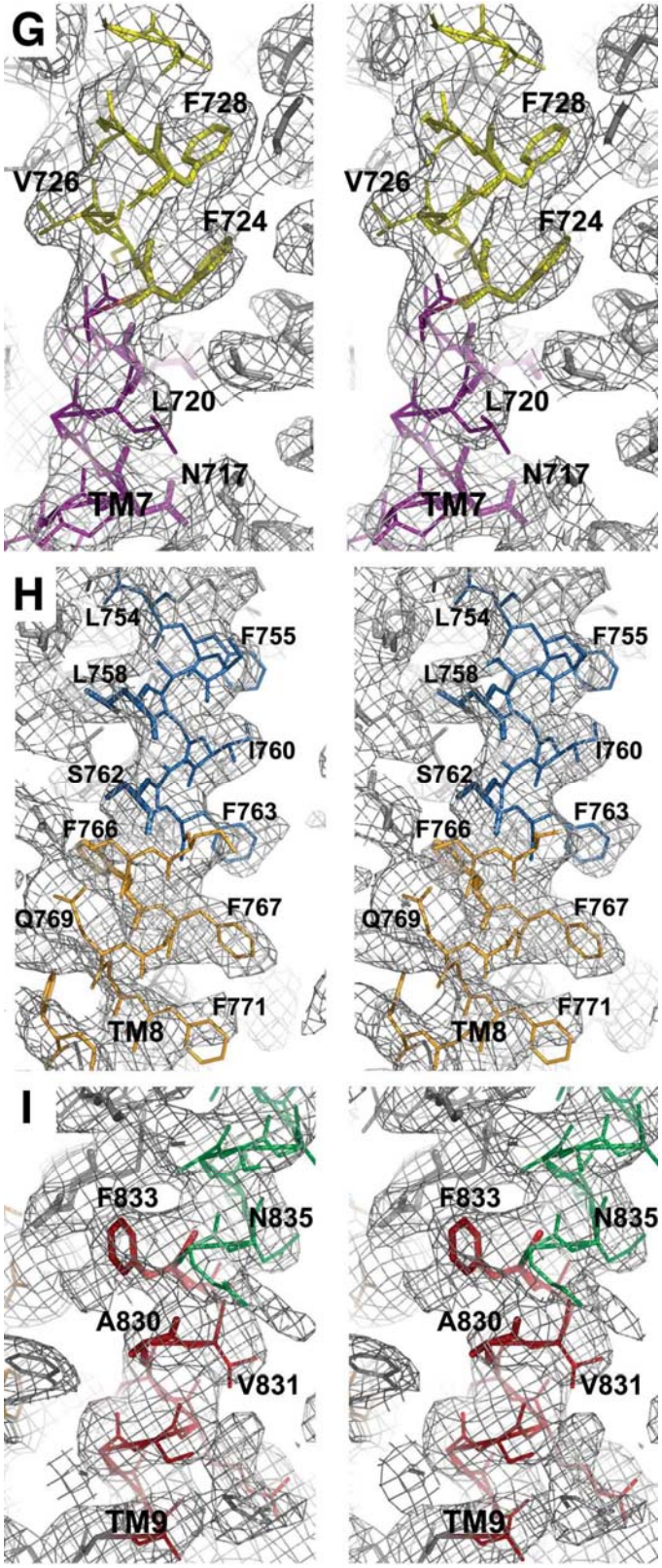
G
F728
V726
F724
L720
N717
TM7
F728
V726
F724
L720
N717
TM7
H
L754
F755
L758
I760
S762
F763
F766
F767
Q769
F771
TM8
L754
F755
L758
I760
S762
F763
F766
F767
Q769
F771
TM8
I
F833
N835
A830
V831
TM9
F833
N835
A830
V831
TM9

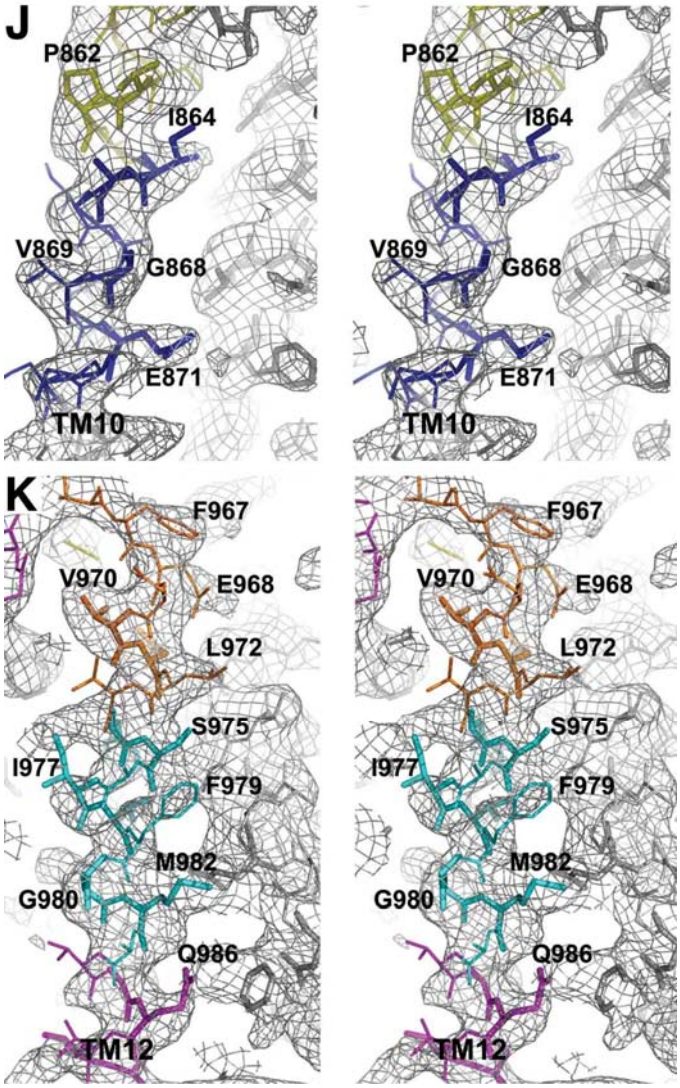
J
P862
I864
V869
G868
E871
TM10
P862
I864
V869
G868
E871
TM10
K
F967
V970
E968
L972
S975
I977
F979
M982
G980
Q986
TM12
F967
V970
E968
L972
S975
I977
F979
M982
G980
Q986
TM12

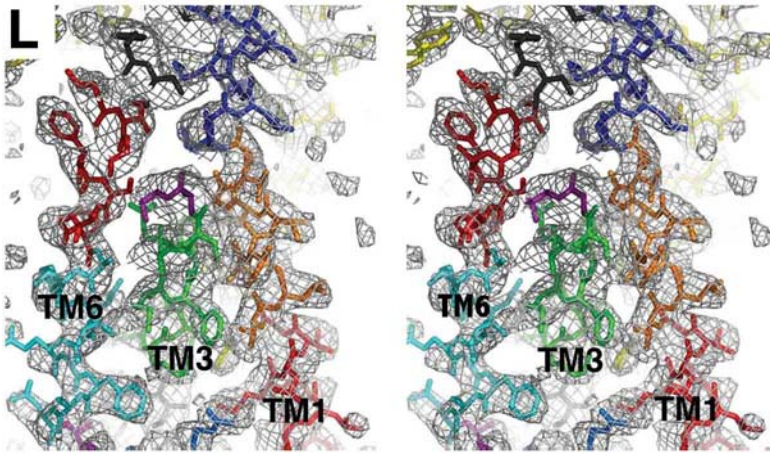

Fig. S9. (A-K) Stereo view of Fo-Fc density for TM helices 1-12 of apo-Pgp with multiple Fo-Fc density maps superimposed. (L) Stereo view of the packing of TMs 1, 3 and 6 of apo-Pgp with multiple Fo-Fc density maps superimposed. The maps were obtained exactly as described for Fig. S8.

Fig. S10

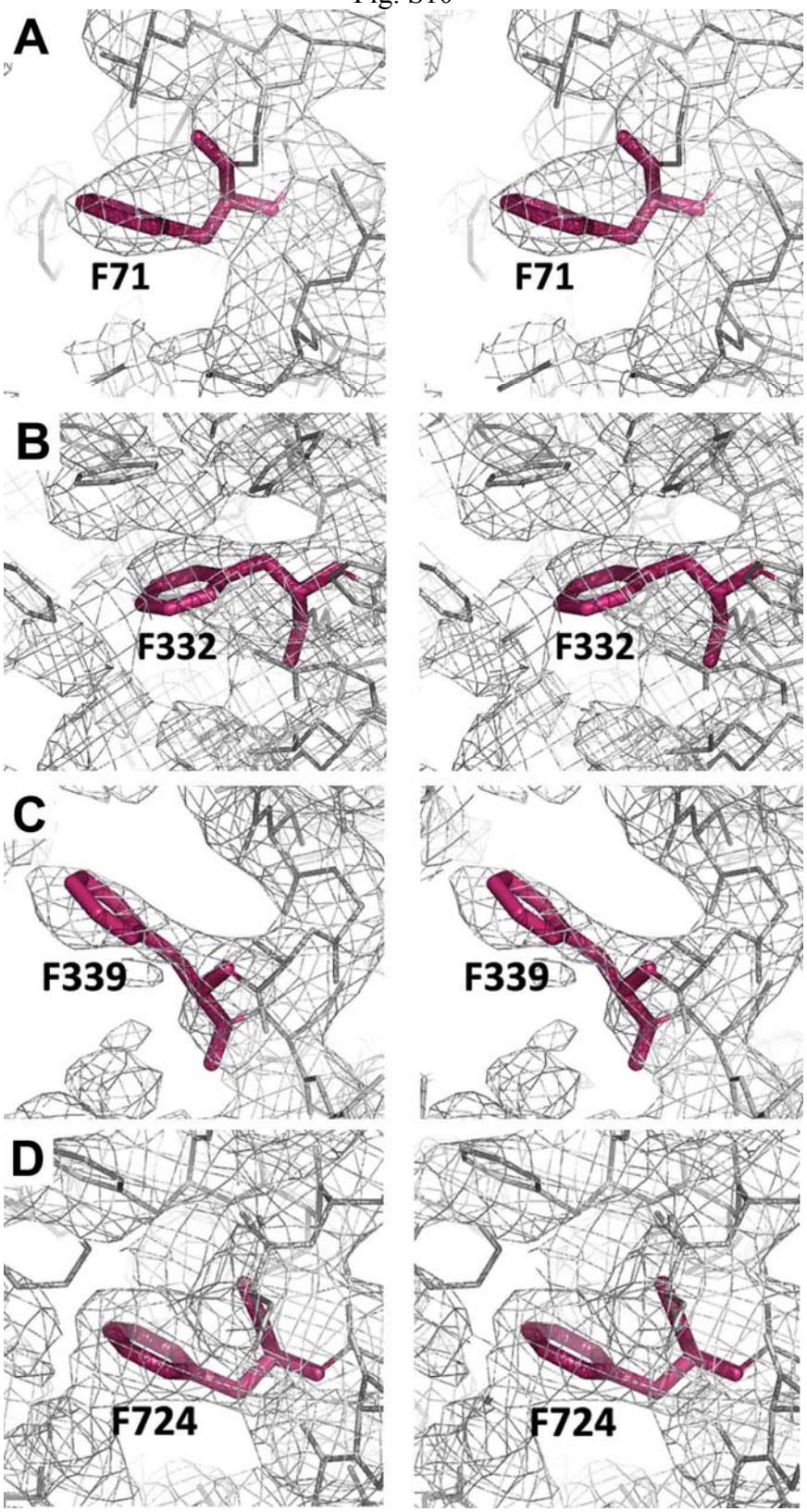

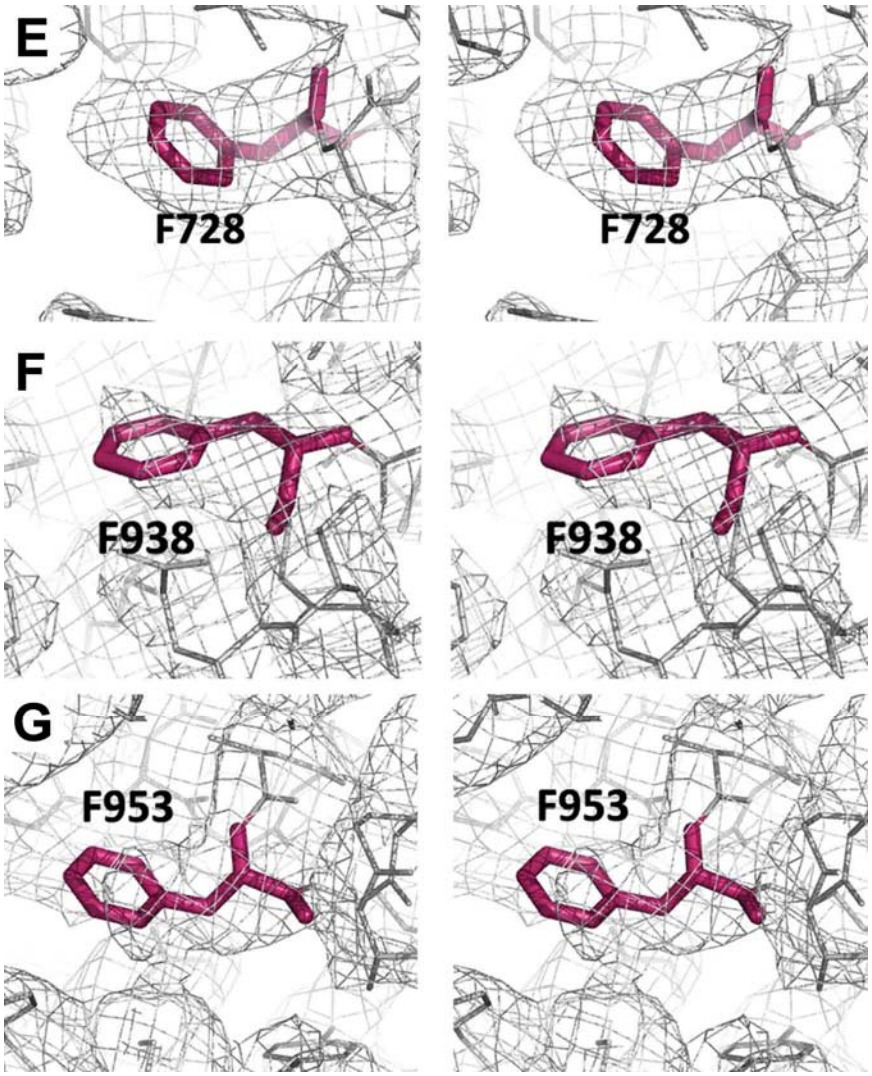

Fig. S10. Fo-Fc analysis of apo-Pgp. (A-G) Fo-Fc density of selected aromatic amino acids in the internal cavity. Residues F332 (B), F339 (C), F724 (D), F728 (E), and F938 (F) play important roles in drug-contact for QZ59 cyclic peptides (this study) or verapamil (previous studies). Fo-Fc density was obtained exactly as described for Fig. S8.

Fig. S11

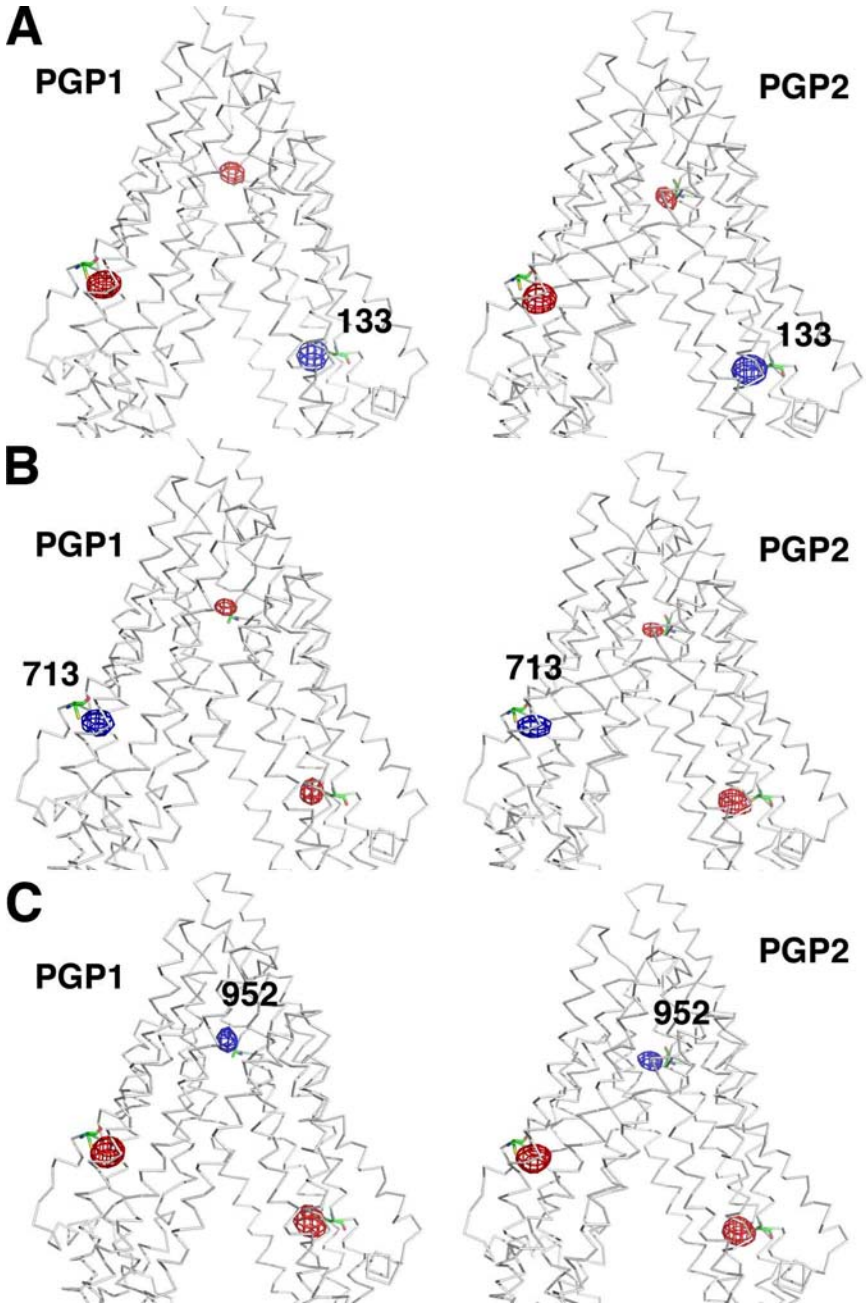

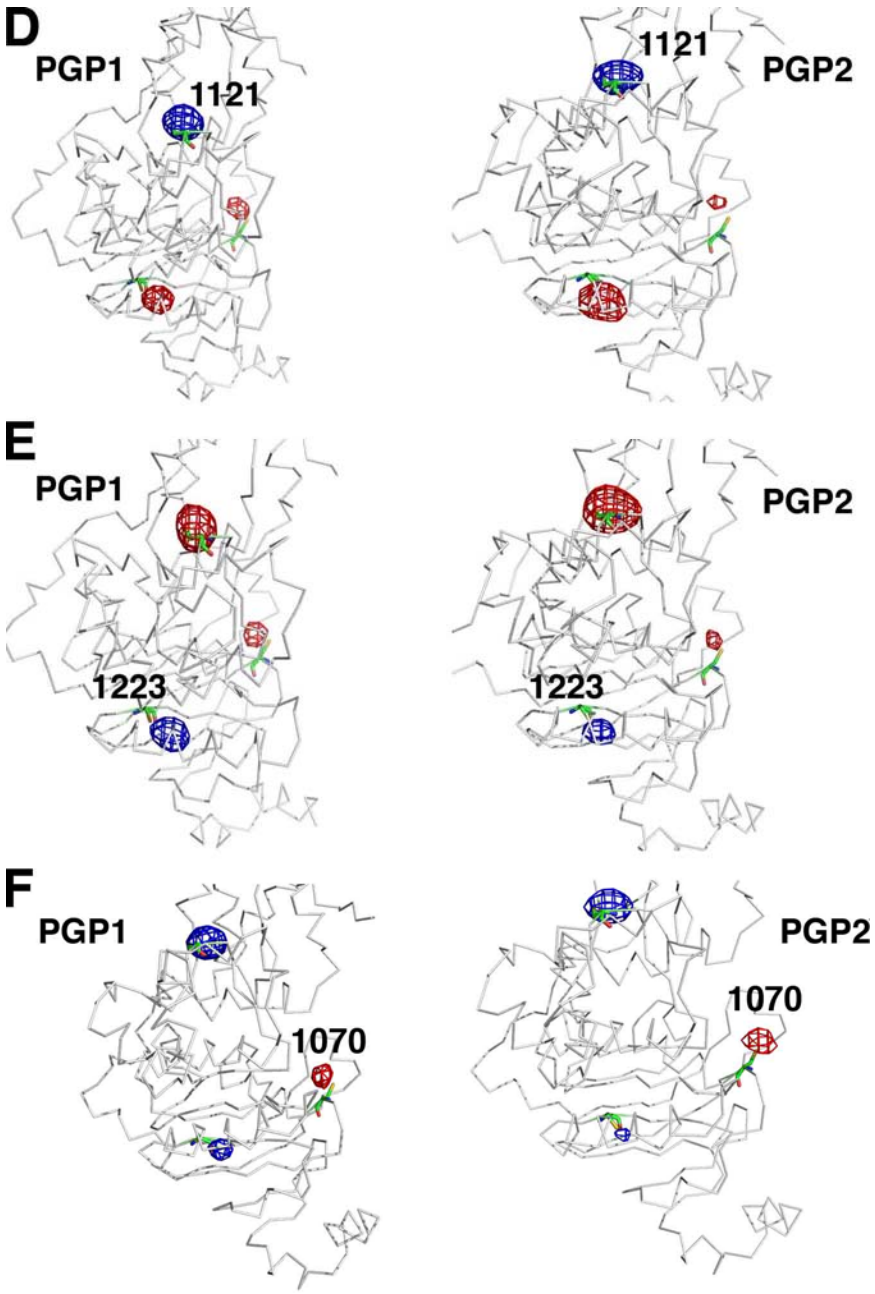
D
PGP1
1121
1121
PGP2
E
PGP1
1223
PGP2
1223
F
PGP1
1070
PGP2
1070

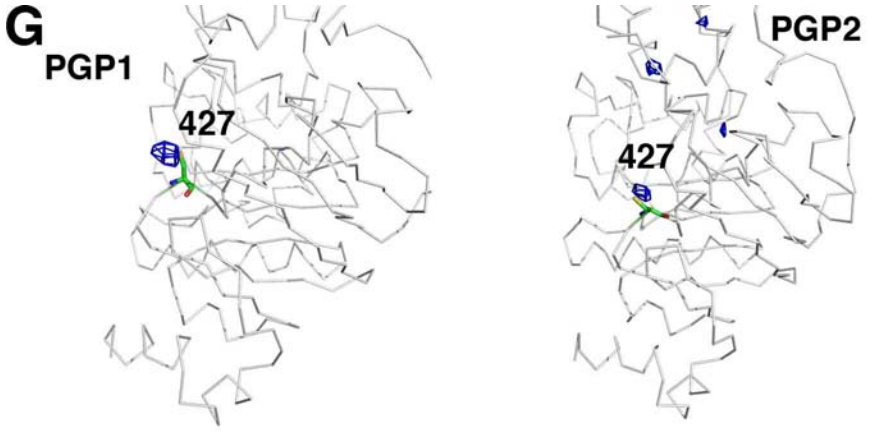

Fig. S11. Verification of Pgp topology. Close-up views of isomorphous- and anomalous-difference Fourier maps superimposed on the Pgp model for seven different cysteine point mutants to confirm the position and identity of residues. The results for both molecules in the asymmetric unit, PGP1 and PGP2, are shown. (A) C133A, (B) C713A, (C) C952A, (D) C1121A, (E) C1223A, (F) Cysless1070C, and (G) C427A. Isomorphous difference maps for each mutant were calculated exactly as described in Fig. 7C. Isomorphous difference peaks (blue) indicate the positions of the Hg for residues mutated to alanine. Anomalous difference Fourier peaks (red) show Hg positions for all other cysteines except the residue changed to alanine, which should be absent. To verify the position and identity of C1070, a single cysteine at position 1070 was introduced using a cysless mutant (*31*) of Pgp (F). For this mutant, the anomalous Fourier shows a Hg peak binding C1070 while the isomorphous difference Fourier with the C952A dataset indicates the position of other CMNP labeled cysteines (G). C427 is the only cysteine in NBD1. All peaks are contoured at 5-7σ, except for C427A PGP2, which is contoured at 3σ.

Fig. S12

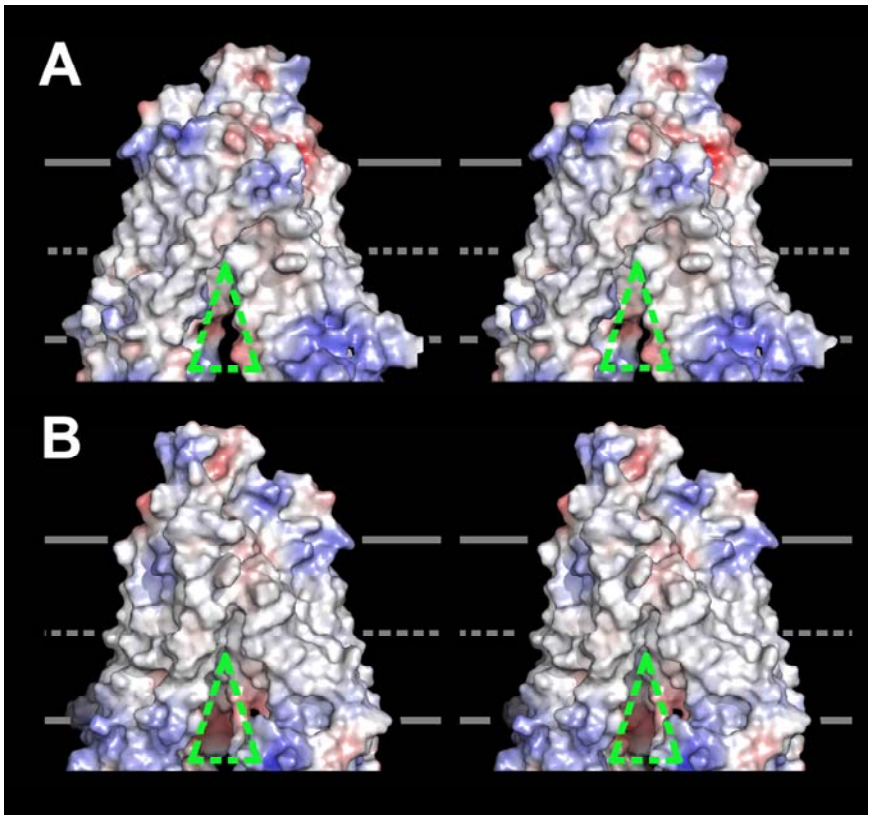

Fig. S12. Pgp drug-entry portals. (A) Stereo-view of Pgp electrostatic surface within the lipid bilayer. (B) View rotated 180^{o} from (A) showing the portal on the opposite side of Pgp. Solid lines delineate the approximate location of lipid headgroups and dashed line represents the ends of the lipid acyl chains halfway through the bilayer. The surface of Pgp is colored according to variation from blue (positively charged regions) to white (hydrophobic and aromatic) to red (negatively charged regions). A green triangle highlights the opening of the portal.

Fig. S13

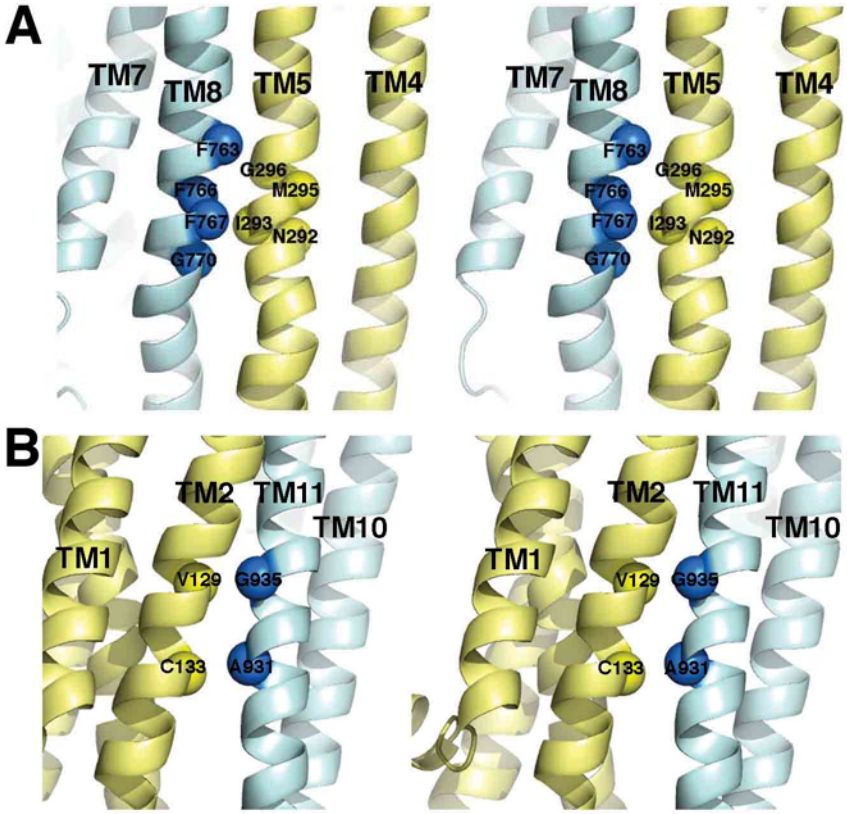

Fig. S13. Support of the intertwined interface structure by previous crosslinking studies. Mouse Pgp positions are displayed as spheres corresponding to human Pgp residues identified by cysteine-scanning and copper phenanthroline crosslinking in the absence of nucleotide and drugs. These positions on (A) TM5 and TM8 could cross link with each other (*32*) as well as those on (B) TM2 and TM11 (*33*).

Fig. S14

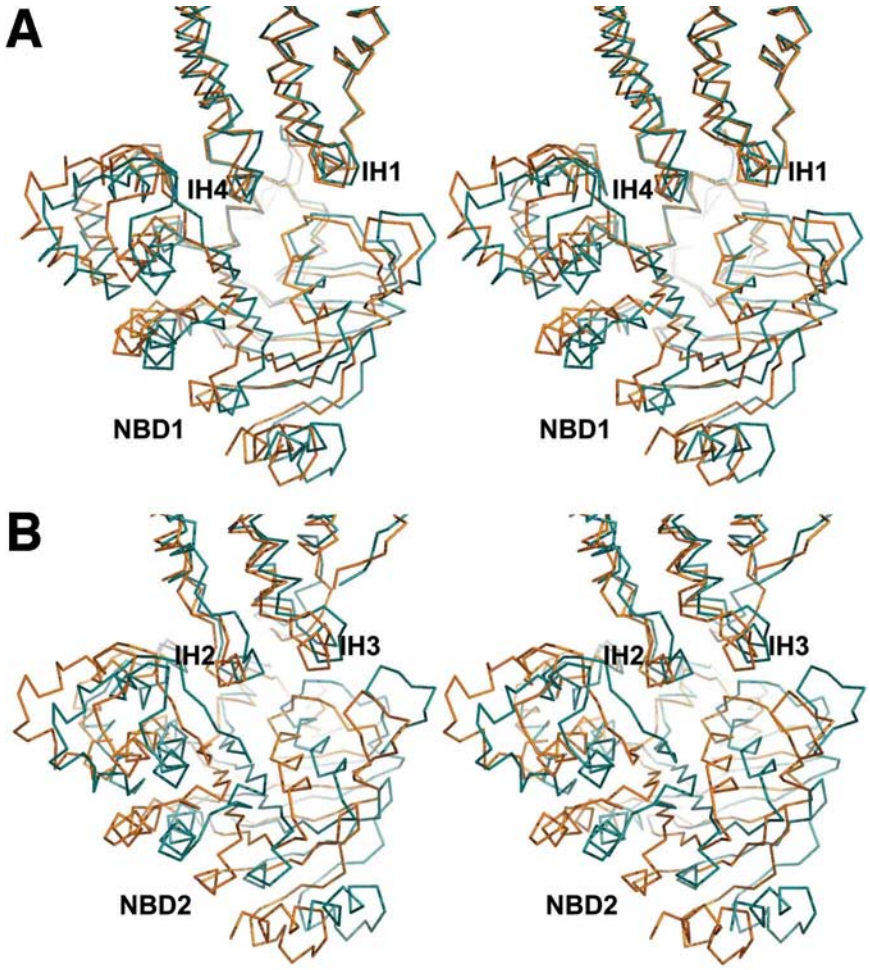

Fig. S14. Comparison of PGP1 and PGP2 conformations in the asymmetric unit. A displacement of NBDs is apparent when the transmembrane domains are aligned (0.7 Å rmsd of Cα atoms). (A) Stereo view looking toward NBD1 from the opposing NBD2. PGP1 is rendered in cyan ribbon, and PGP2 is rendered orange. (B) Stereo view looking toward NBD2 from the apposing NBD1; same coloring scheme. The x-ray structures of each drug-bound form (QZ59-RRR and QZ59-SSS) are superimposable to apo and also to each other (0.7 Å rmsd of C_α atoms)**.**

Fig. S15

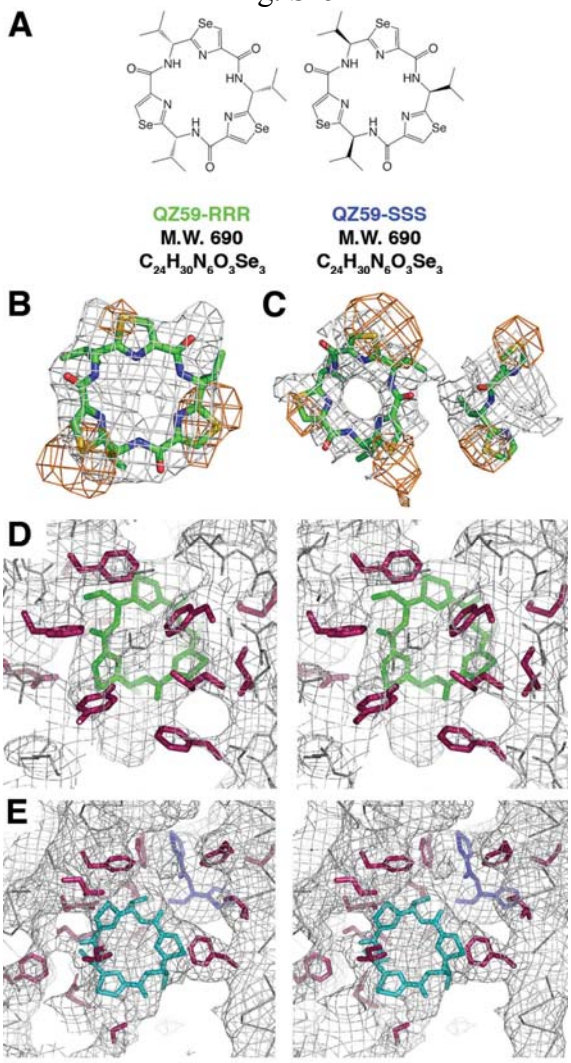

Fig. S15. QZ59 inhibitor binding. (A) Chemical structures of QZ59-RRR and QZ59-SSS. (B) QZ59-RRR molecule and Fo-Fc density (gray mesh) calculated using a Pgp model lacking the cyclic peptide molecule. The location of the QZ59-RRR was verified by anomalous Fourier peaks (orange mesh) corresponding to selenium atoms in the QZ59-RRR model as shown in (A). (C) Fo-Fc density (gray mesh) and anomalous Fourier peaks (orange mesh) for both QZ59-SSS molecules. A portion of the QZ59-SSS molecule occupying the "upper" site is less ordered as indicated by partial coverage of the difference density and a missing Se peak. This region of the ligand is absent in both copies of Pgp in the asymmetric unit and is likely caused by the flexibility of the hydrophobic and non-polar residues on the extracellular side of the “upper” site. All anomalous Fourier peaks for selenium are contoured at 4.5σ. Fo-Fc density, calculated omitting a neighboring sphere of 2 Å, is contoured at 3σ for (B) and 1σ for (C). (D) Stereo view showing QZ59-RRR molecule (green sticks) and neighboring residues (magenta sticks). (E) Stereo view of two QZ59-SSS molecules (blue and cyan sticks) and surrounding residues (magenta sticks). Fo-Fc density (gray mesh) in both (D) and (E) was obtained in the same manner as Fig S8. Cα trace of backbone is in dark gray. Fo-Fc density for (D) and (E) is contoured at 2σ.

Fig. S16

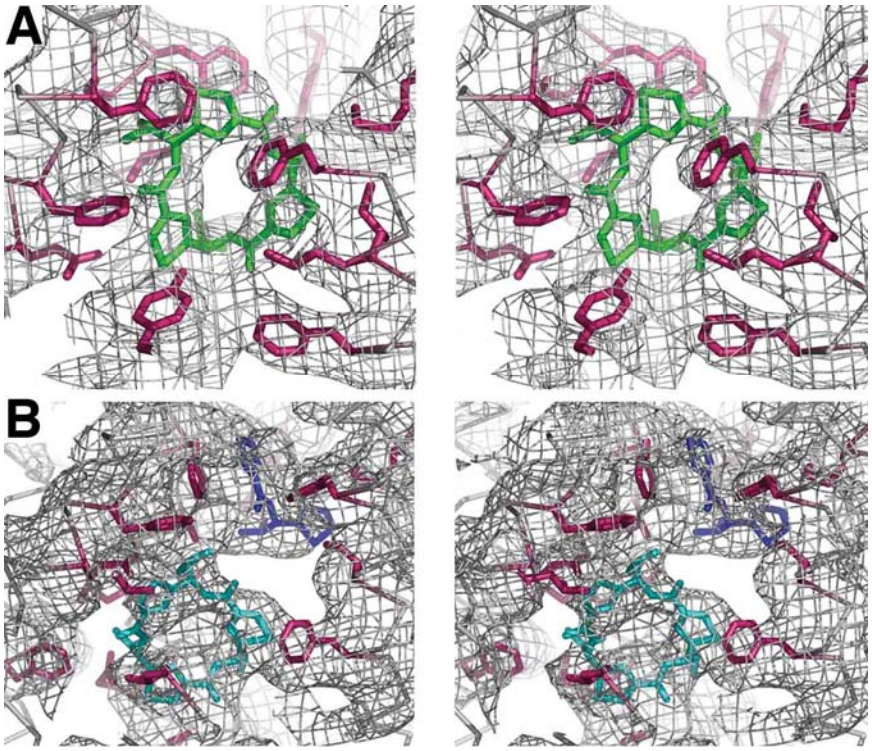

Fig. S16. Fo-Fc density of Pgp QZ59-binding sites omitting only the surrounding residues and ligands. (A) Fo-Fc density for the QZ59-RRR molecule and surrounding residues was generated by omitting the inhibitor molecule (green) and residues (red) that are in close proximity to the inhibitor (residues 68, 303, 332, 335, 336, 339, 721, 724, 728, 949, 974, and 975). (B) The same procedure was used to calculated the Fo-Fc density for the QZ59-SSS drug-binding site omitting both inhibitors and surrounding residues (residues 64, 67, 68, 71, 300, 303, 311, 332, 336, 339, 721, 724, 728, 833, 949, 971, 977, 974, 978, 985, and 989). All Fo-Fc density is unsharpened and contoured at 1s (CNS v1.2). This difference density is nearly super-imposable with that shown in Fig. S15D and E.

Fig. S17

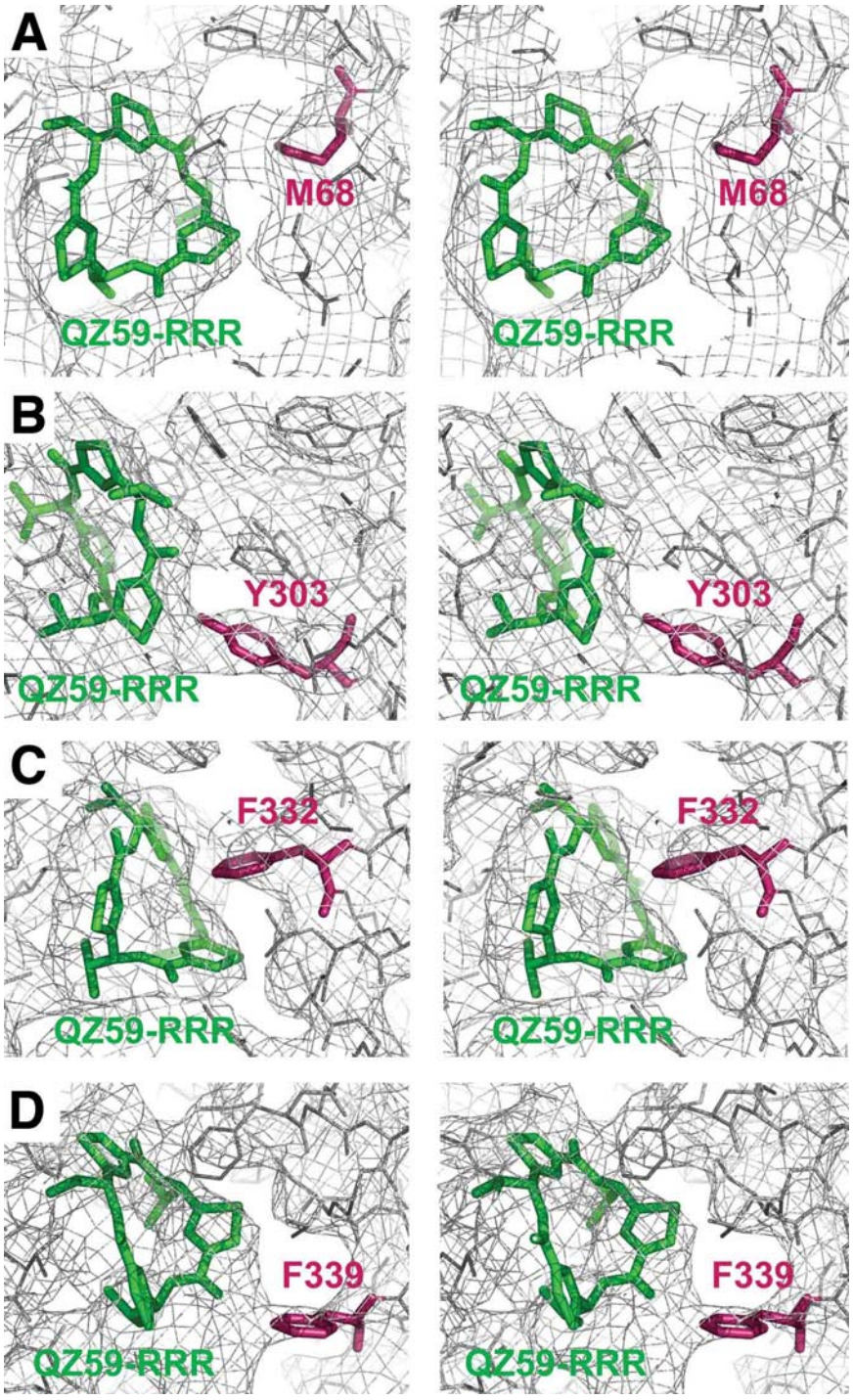
A
M68
QZ59-RRR
M68
QZ59-RRR
B
Y303
QZ59-RRR
Y303
QZ59-RRR
C
F332
QZ59-RRR
F332
QZ59-RRR
D
F339
QZ59-RRR
F339
QZ59-RRR

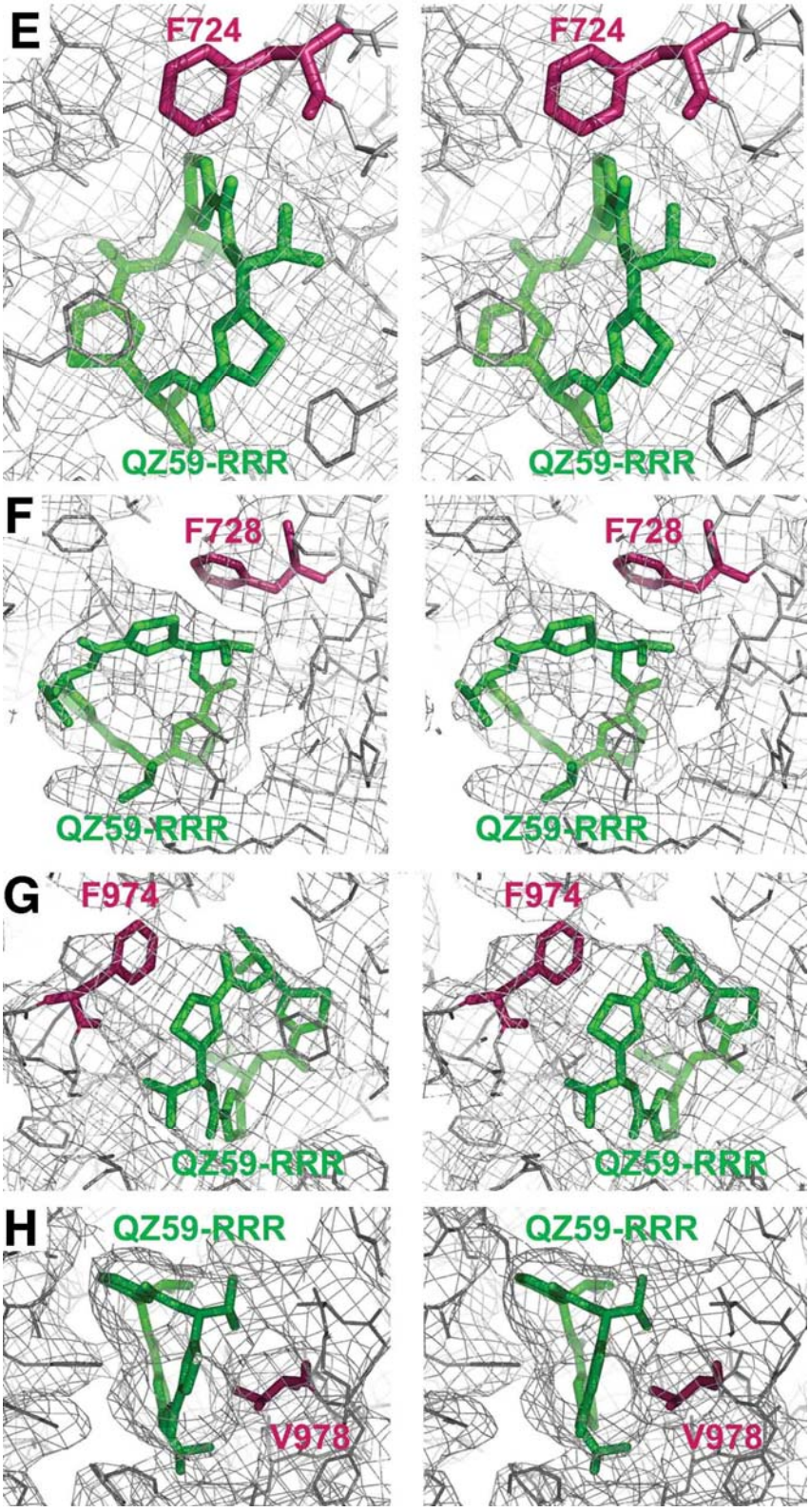
E
F724
QZ59-RRR
F724
QZ59-RRR
F
F728
QZ59-RRR
F728
QZ59-RRR
G
F974
QZ59-RRR
F974
QZ59-RRR
H
QZ59-RRR
V978
QZ59-RRR
V978

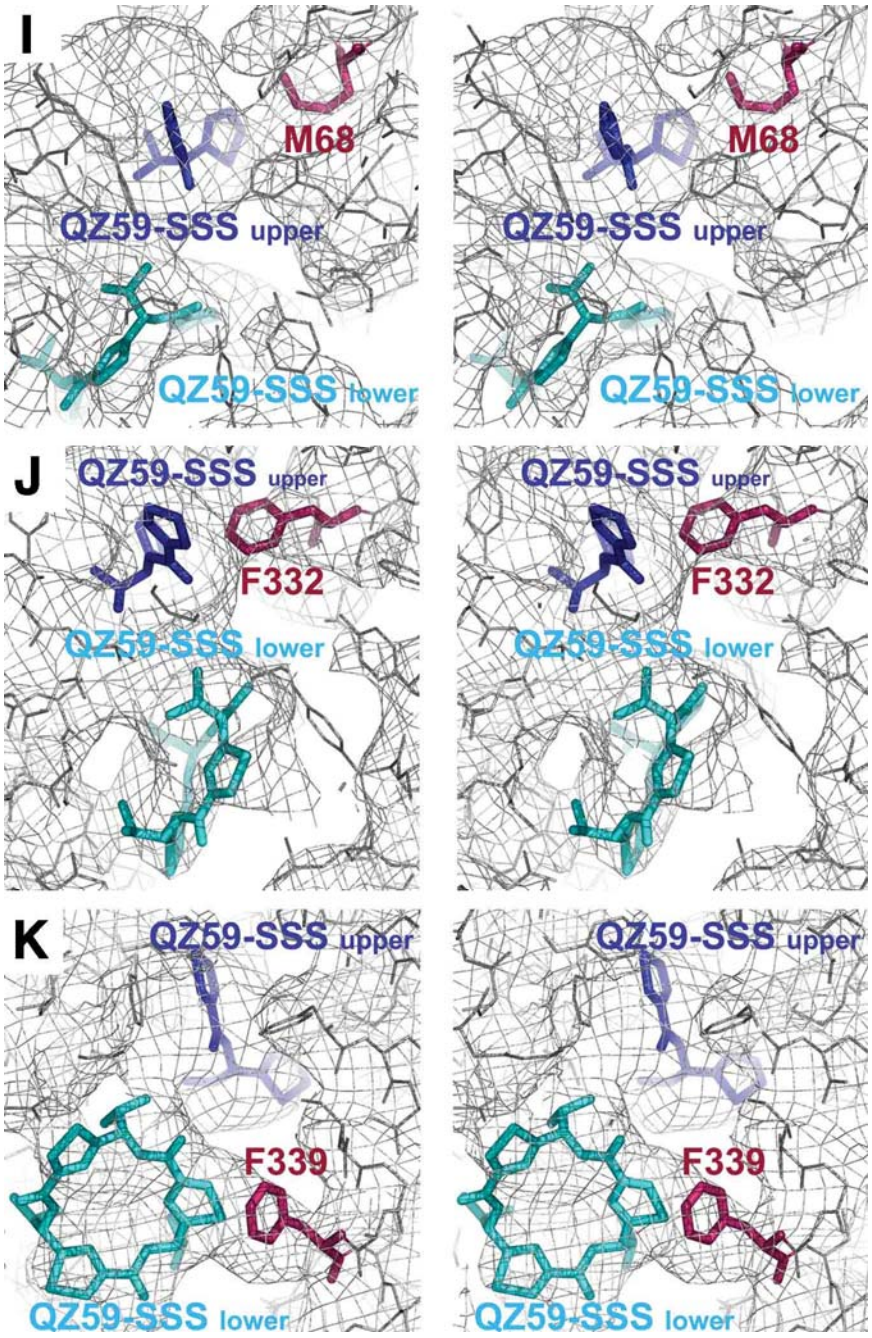
I
M68
QZ59-SSS upper
QZ59-SSS lower
M68
QZ59-SSS upper
QZ59-SSS lower
J
QZ59-SSS upper
F332
QZ59-SSS lower
QZ59-SSS upper
F332
QZ59-SSS lower
K
QZ59-SSS upper
F339
QZ59-SSS lower
QZ59-SSS upper
F339
QZ59-SSS lower

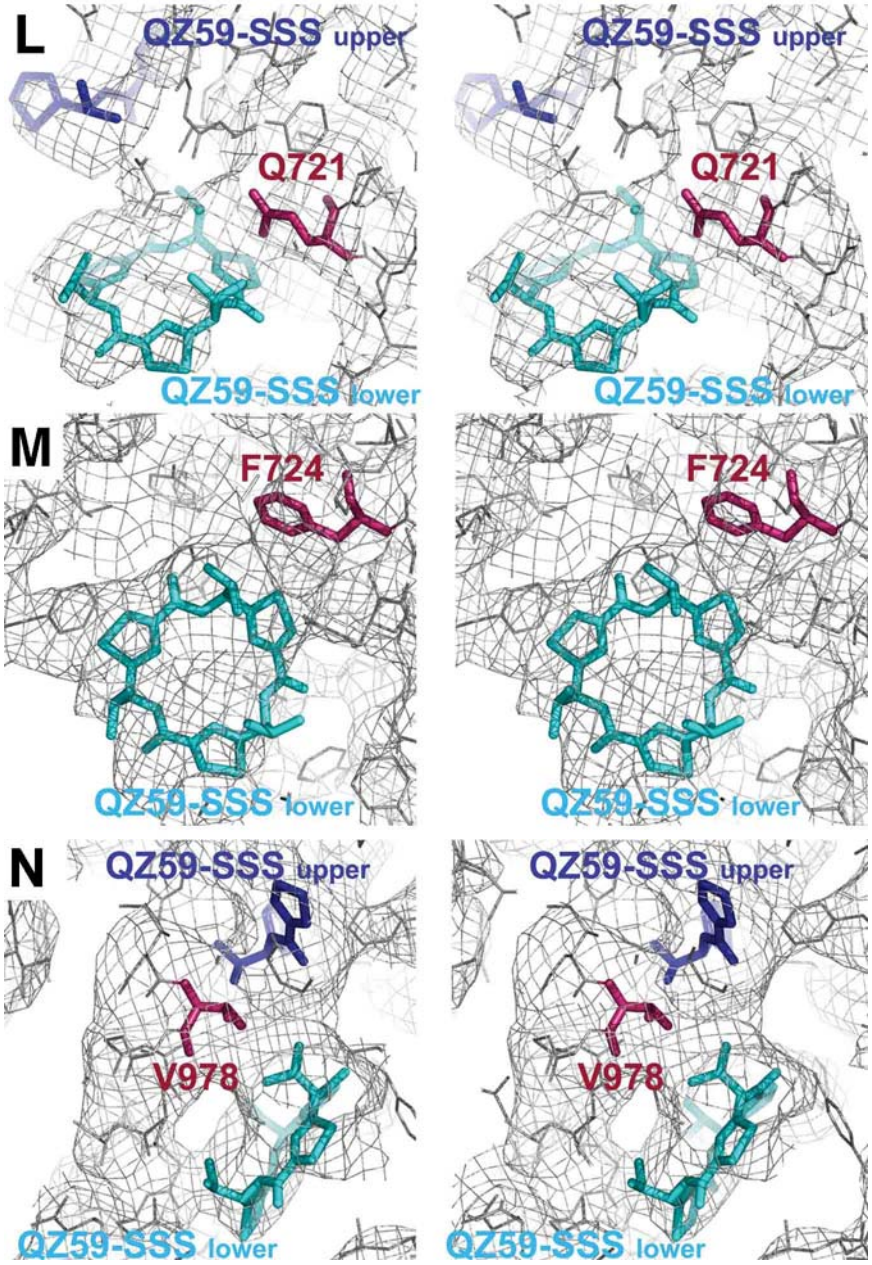

Fig. S17. Fo-Fc density of QZ59 compounds and surrounding residues. The difference density for the ligand and surrounding residues are shown for the (A-G) QZ59-RRR and (H-M) QZ59-SSS co-crystal structures. The QZ59-RRR molecule is shown in green while the QZ59-SSS molecule in the "lower" and "upper" site are shown in blue and cyan, respectively. Pgp residues in close proximity to the inhibitors are shown in red with labels. All Fo-Fc density (grey) is generated as described in Fig. S8 and the difference maps for the ligands were generated by omitting them individually. Fo-Fc maps were contoured at 2σ with a B-factor of -50 $Å^2$ applied to the structure factors (CNS v1.2).

Fig. S18

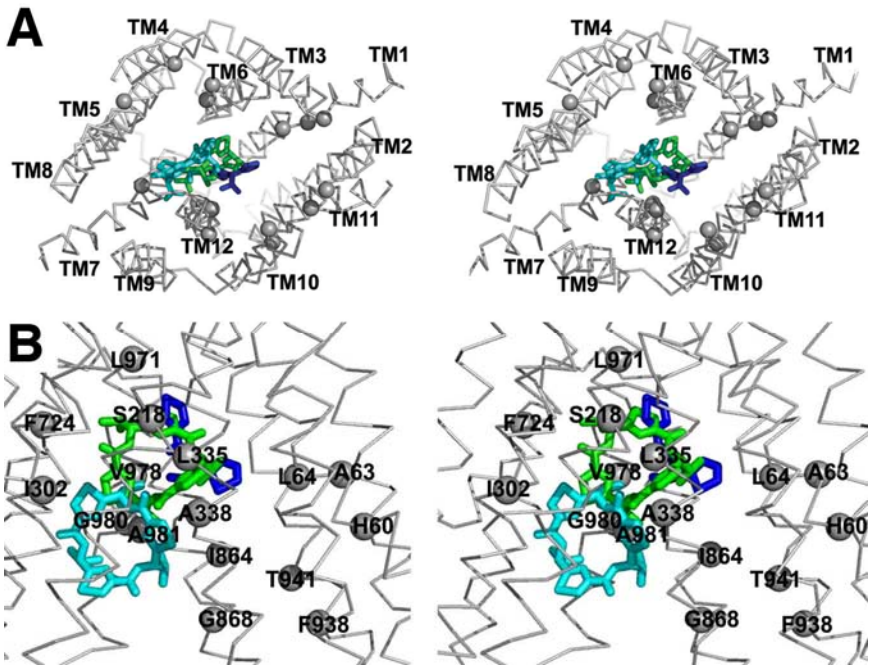

Fig. S18. Location of residues protected from MTS labeling by verapamil (*26-30*). These residues are interpreted as those that interact with verapamil. (A) Stereo view from intracellular side of QZ59 compounds with verapamil-interacting residues shown as grey spheres on the Apo-Pgp structure (grey backbone). The relative position of the ligands from the co-crystal structures of Pgp with QZ59-SSS and QZ59-RRR are superimposed, suggesting that the "middle", "upper", and "lower" (green, blue and cyan, respectively) QZ59 binding sites overlap with the binding site for verapamil. (B) View rotated 90˚ from (A) with all verapamil-interacting residues numbered according to their positions on mouse Pgp (Fig. S1).

Fig. S19

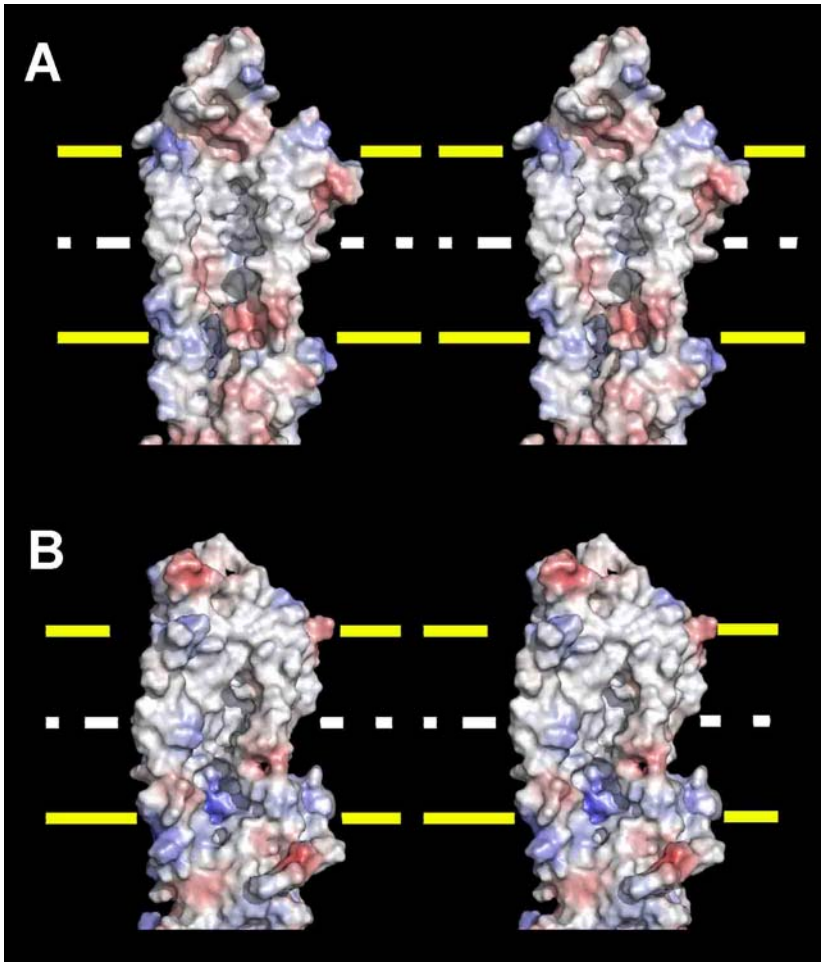

Fig. S19. Electrostatic potential surface of drug binding pocket. (A) N-terminal and (B) C-terminal half views of internal chamber of Pgp colored by electrostatic potential (blue is positive, red is negative, and white is neutral). The putative location of the bilayer is delineated by the solid yellow and white dashed lines. In Pgp, the internal chamber is charged at the bottom of the inner leaflet and becomes more hydrophobic/aromatic toward the outer leaflet of the membrane. The QZ59 compounds bind in the hydrophobic/aromatic region of the pocket. The panels are oriented with the extracellular side at the top.

Fig. S20

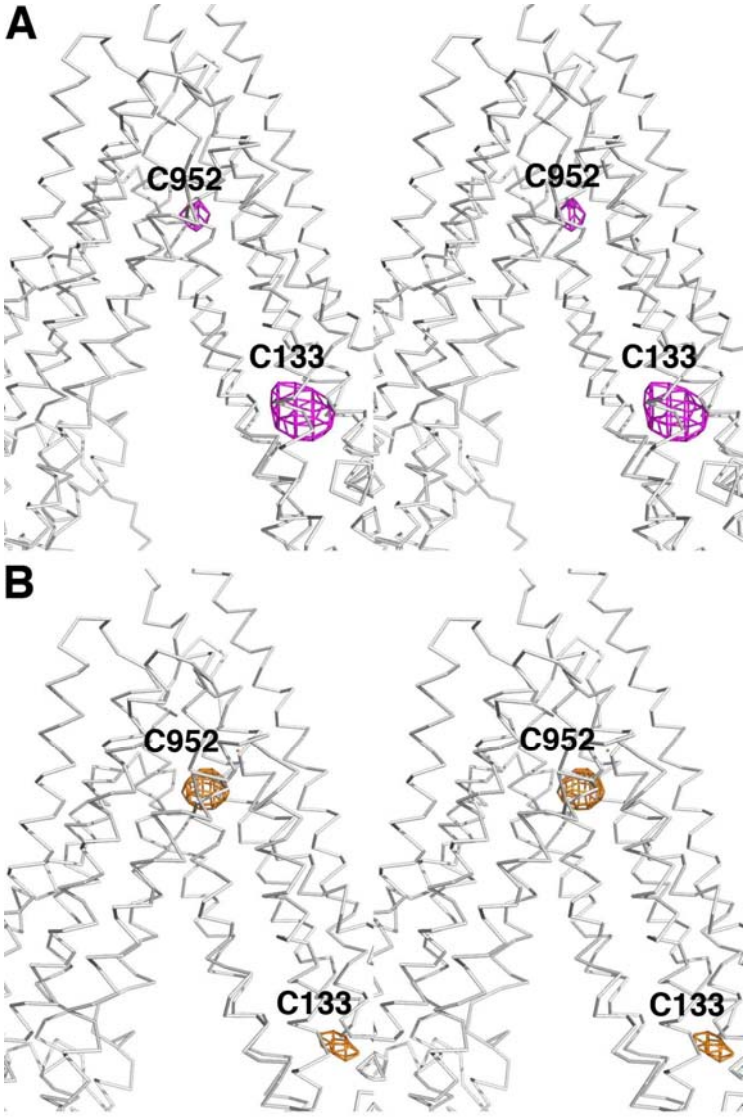

Fig. S20. Binding of small hydrophobic heavy metal compounds to pre-formed Pgp crystals. Anomalous difference Fourier electron density for (A) ethylmercury chloride (255 Da; magenta) and (B) tetramethyl lead (267 Da; orange) soaks, each contoured at 4σ. The labeling of Cys952 deep within the drug binding pocket demonstrates the ability of these small hydrophobic compounds to penetrate deep into the drug binding pocket. In contrast, the larger QZ59 compounds (660 Da) cannot enter into the drug binding pocket once this particular conformation has been formed as indicated by the lack of difference density or selenium anomalous peaks. This result suggests that a more open inward facing conformation may be required for binding larger compounds.

Fig. S21

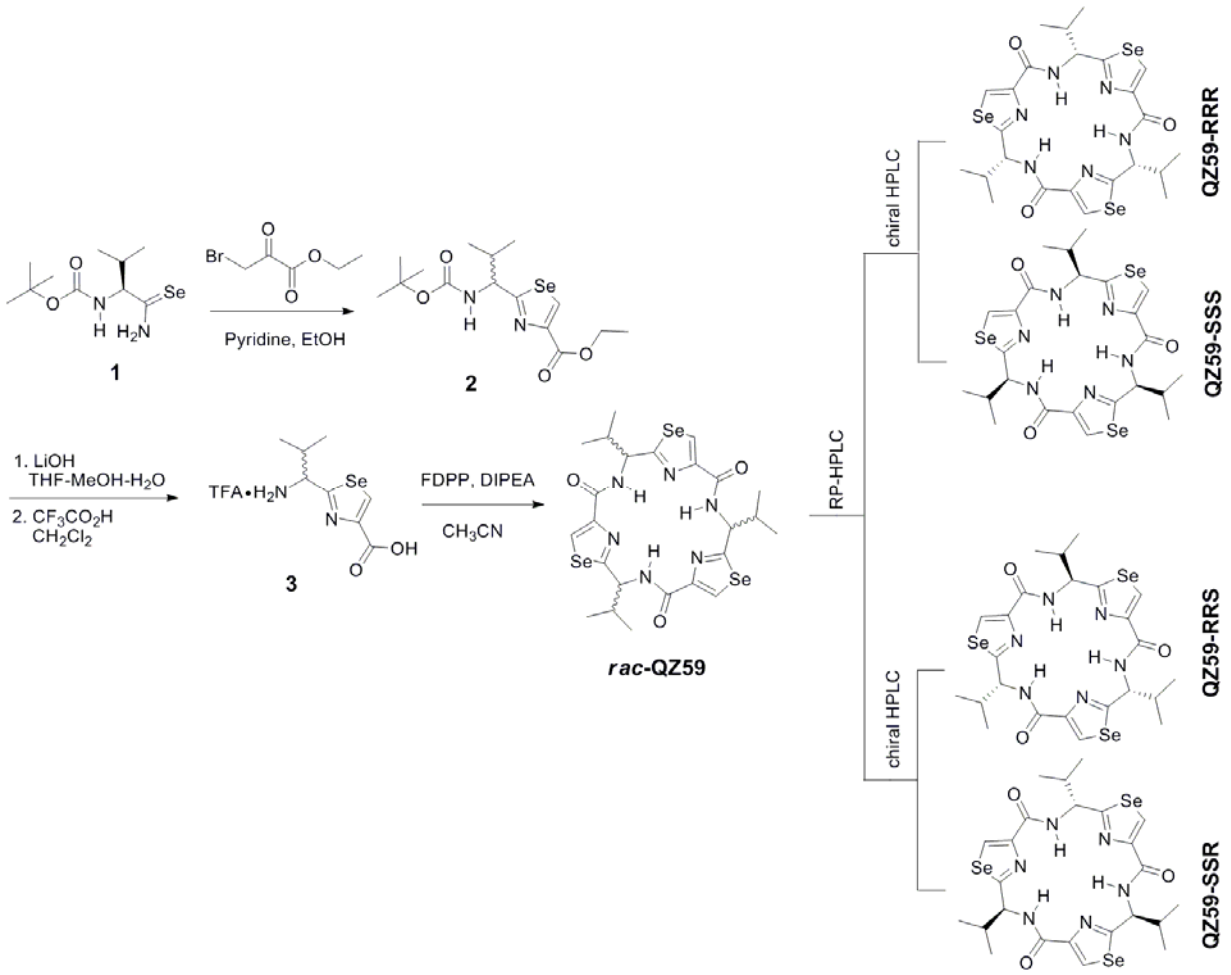

Fig. S21. Synthesis of cyclic hexapeptide inhibitors of Pgp. QZ59-RRR and QZ59-SSS were isolated by sequential RP-HPLC and chiral HPLC column purification.

Table S1. Crystallographic Table.

Data Processing	Crystal 1		Crystal 2 (C952A)		QZ59-RRR	QZ59-SSS
Source	SSRL 11-1		APS 23-ID-B		APS 23-ID-D	SSRL 11-1
Space Group	$P\ 2_12_12_1$		$P\ 2_12_12_1$		$P\ 2_12_12_1$	$P\ 2_12_12_1$
Unit Cell	a=99.0 Å, b=119.3 Å, c=381.3 Å, α= β= γ=90.0°		a=97.5 Å, b=115.4 Å, c=378.8Å, α= β= γ=90.0°		a=96.6 Å, b=115.1 Å, c=374.2 Å, α= β= γ=90.0°	a=97.7 Å, b=115.0Å, c=375.8 Å, α= β= γ=90.0°
	E1	E2	E1	E2		
Wavelength (Å)	1.0057	1.0087	1.00695	1.00923	0.97942	0.97854
Resolution (Å)	4.5	4.5	3.8	4.1	4.4	4.35
Redundancy	14.7	14.7	7.9	7.9	3.7	4.0
R_{sym}[a,b], %	0.104 (0.318)	0.098 (0.341)	0.082 (0.378)	0.085 (0.356)	0.073 (0.288)	0.057 (0.382)
Completeness, % ()[b]	94.7 (90)	94.4 (89.3)	96.1 (86.5)	94.8 (87.1)	94.7 (90.3)	93.3 (84.0)

Phasing and map generation	Crystal 1	Crystal 2 (C952A)
Overall Phasing Power	3.1	1.32
Figure of Merit	0.712	0.434

Model Building and refinement	Crystal 2 (C952A)	QZ59-RRR	QZ59-SSS
Resolution, Å	3.8	4.4	4.35
Sigma cutoff	0.0	0.0	0.0
R_{cryst}[c], %/ R_{free}[d], %	30.6/34.7	31.4/36.4	30.8/35.6
Completeness, % ()[b]	96.1(86.8)	94.7(90.1)	93.3(85.3)
Rmsd[e] bond lengths, Å	0.01	0.008	0.008
Rmsd bond angles, deg	1.9	1.5	1.6
<B>, $Å^2$	136.2	198.8	182.3
R_{shrink}, R_{probe} (Å)	0.5, 0.5	0.5, 0.5	0.6, 0.6
Bulk Solvent Param: K, B_{sol} ($Å^2$)	0.2, 68	0.25, 119.9	0.15, 23

[a] $R_{sym} = \Sigma|I-\langle I\rangle|\Sigma\langle I\rangle$, where I is the measured intensity of each reflection, and <I> is the intensity averaged from symmetry equivalents.
[b] High resolution bins: Crystal 1 (4.66-4.5 Å), Crystal 2 (3.94-3.8 Å), QZ59-RRR (4.56-4.4 Å), QZ59-SSS (4.5-4.35 Å).
[c] $R_{cryst} = \Sigma|F_o-F_c|/\Sigma|F_c|$, where F_o and F_c are observed and calculated structure factors, respectively.
[d] R_{free} was calculated from a subset of data (10%) omitted from the refinement.
[e] Rmsd, root mean square deviation.

Table S2. Crystallographic Table.

Data Processing	C133A	C427A	C713A	C952A	Cysless1070C	C1121A	C1223A
Source	ALS 8.2.2	SSRL 9-2	ALS 8.2.2	APS 23-ID-B	SSRL 9-2	APS 23-ID-B	ALS 8.2.2
Unit Cell	a=98.4 Å, b=114.6 Å, c=376.6 Å,	a=97.0 Å, b=116.4 Å, c=377.4 Å,	a=98.4 Å, b=115.4 Å, c=377.6 Å,	a=97.5 Å, b=115.4Å, c=378.8 Å,	a=96.3 Å, b=113.3 Å, c=373.8 Å,	a=97.3 Å, b=115.4 Å, c=376.0 Å,	a=97.5 Å, b=113.5 Å, c=376.3 Å,
Wavelength (Å)	1.0064	1.0063	1.0064	1.0070	1.0053	1.0070	1.000
Resolution (Å)	4.9	4.1	4.1	3.8	4.5	5.0	5.0
Redundancy	4.7	4.1	3.8	7.7	3.8	7.3	3.6
R_{sym}[a], %	7.6	6.9	7.6	7.2	11.3	8.5	9.1
Completeness, %	89	92	88	96	89	95	84

[a] $R_{sym} = \Sigma|I-\langle I\rangle|\Sigma\langle I\rangle$, where I is the measured intensity of each reflection, and <I> is the intensity averaged from symmetry equivalents.

Table S3.

TM	Residue	QZ59-RRR	QZ59-SSS	Verapamil	TM	Residue	QZ59-RRR	QZ59-SSS	Verapamil
1	His 60			x	7	Asn 717			
	Gly 61					Gln 721	x	x	
	Ala 63			x		Phe 724	x	x	x
	Leu 64			x		Phe 728	x		
	Pro 65				8	Leu 758		x	
	Met 67					Ser 762			
	Met 68	x	x			Phe 766			
	Phe 71				9	Ala 830			
2	Tyr 110					Phe 833		x	
	Tyr 113				10	Ile 860			
	Val 121					Val 861			
3	Gly 187					Ile 864			x
	Phe 190					Ala 865			
	Gln 191					Ala 867			
	Ala 194					Gly 868			x
4	Gly 222					Glu 871			
	Ala 225				11	Phe 938			x
	Ala 229					Thr 941			
	Ser 233					Gln 942			
5	Gly 296					Met 945			
	Phe 299					Ser 948			
	Leu 300		x			Tyr 949	x	x	
	Tyr 303	x	x			Ala 952			
	Tyr 306					Phe 953			
	Phe 310				12	Val 970			
	Trp 311					Leu 971			x
6	Leu 328					Phe 974	x	x	
	Thr 329					Ser 975	x		
	Phe 332	x	x			Val 978	x	x	x
	Ser 333					Gly 980			x
	Leu 335	x		x		Ala 981		x	x
	Ile 336	x	x			Met 982		x	
	Ala 338			x		Gly 985		x	
	Phe 339	x	x			Gln 986		x	
	Gly 342					Ser 988			
	Gln 343					Ser 989		x	
	Pro 346								

Table S3. Residues facing the internal cavity of Pgp within the lipid bilayer for the apo PGP1 structure (Crystal2). The residues in TM helices are indicated. Residues that interact with QZ59-RRR and QSZ59-SSS models, as well as those protected by MTS-verapamil labeling by verapamil **(*26-30*)** are marked.

Table S4.

	QZ59-RRR	cyclic-tris-(*R*)-valinethiazole	QZ59-SSS	cyclic-tris-(*S*)-valinethiazole
$[\alpha]^{20}_{D}$ [a]	+65.8	+105.1	-65.1	-107.1
RT (min) [b]	12.7	9.8	10.2	8.5

[a] Determined on Perkin-Elmer 343 polarimeter using $CHCl_3$ as the solvent.
[b] Determined by chiral HPLC using chiralcel OD-H column (4.6 cm x 250 cm) eluting with 1:3 isopropanol/hexane.

Table S4. Determination of the absolute configuration of QZ59-RRR and QZ59-SSS by comparing with the authentic thiazole analogues.

Table S5.

Region	Residues	Location	Density Correlation
1.	33-208, 322-368	TMs 1, 2, 3, 6	66%
2.	385-626	NBD1	70%
3.	694-851, 962-1008	TMs 7, 8, 9, 12	67%
4.	1031-1270	NBD2	57%
5.	210-320	TMs 4, 5	72%
6.	853-960	TMs 10, 11	69%

Table S5. Initial density correlation coefficient applying NCS averaging between six regions of PGP1 and PGP2. The mask included a 3 Å cushion around the model. The remaining portions of the model not averaged were incorporated in the mask during solvent flattening.

REFERENCES

1. I. L. Urbatsch, L. Beaudet, I. Carrier, P. Gros, *Biochemistry* **37**, 4592 (Mar 31, 1998).
2. N. Lerner-Marmarosh, K. Gimi, I. L. Urbatsch, P. Gros, A. E. Senior, *Journal of Biological Chemistry* **274**, 34711 (Dec 3, 1999).
3. I. L. Urbatsch, S. Wilke-Mounts, K. Gimi, A. E. Senior, *Archives of Biochemistry & Biophysics* **388**, 171 (Apr 1, 2001).
4. S. G. Aller, V. M. Unger, *Proceedings of the National Academy of Sciences of the United States of America* **103**, 3627 (Mar 7, 2006).
5. T. C. Terwilliger, *Acta Crystallographica Section D-Biological Crystallography* **56**, 965 (Aug, 2000).
6. T. C. Terwilliger, J. Berendzen, *Acta Crystallographica Section D-Biological Crystallography* **55**, 849 (Apr, 1999).
7. W. a. S. S. Furey, *Methods in Enzymology: Macromolecular Crystallography* **277**, Chap 31 (1997).
8. A. T. Brunger *et al.*, *Acta Crystallographica Section D-Biological Crystallography* **54**, 905 (Sep 1, 1998).
9. A. T. Brunger, **Yale University Press, New Haven, CT.** (1992).
10. R. J. P. Dawson, K. P. Locher, *Nature* **443**, 180 (Sep 14, 2006).
11. A. Ward, C. L. Reyes, J. Yu, C. B. Roth, G. Chang, *Proceedings of the National Academy of Sciences of the United States of America* **104**, 19005 (Nov 27, 2007).
12. C. A. Hrycyna *et al.*, *Biochemistry* **37**, 13660 (Sep 29, 1998).
13. T. W. Loo, D. M. Clarke, *Journal of Biological Chemistry* **269**, 7750 (Mar 11, 1994).
14. J. Ogino, R. E. Moore, G. M. Patterson, C. D. Smith, *Journal of Natural Products* **59**, 581 (Jun, 1996).
15. J. S. Sack, *Journal of Molecular Graphics* **6**, 224 (1988).
16. P. Emsley, K. Cowtan, *Acta Crystallographica Section D-Biological Crystallography* **60**, 2126 (Dec, 2004).
17. W. L. DeLano, (2002).
18. K. Geisler, Jacobs, A., Kunzler, A., Mathes, M., Girrleit, I., Zimmermann, B., Bulka, E., Pfeiffer, W. D., and Langer, P., *Synlett*, 1983 (2002).
19. S. Yan, Larson, G., Wu, J. Z., Appleby, T., Ding, Y., Hamatake, R., Hong, Z., and Yao, N., *Bioorganic & Medicinal Chemistry Letters* **17**, 63 (2007).
20. A. Bertram, Blake, A. J., de Turiso, F. G. L., Hannam, J. S., Jolliffe, K. A., Pattenden, G., and Skae, M, *Tetrahedron* **59**, 6979 (2003).
21. R. Callaghan, G. Berridge, D. R. Ferry, C. F. Higgins, *Biochimica et Biophysica Acta* **1328**, 109 (Sep 4, 1997).
22. G. Vogel, R. Steinhart, *Biochemistry* **15**, 208 (Jan 13, 1976).
23. I. L. Urbatsch, B. Sankaran, J. Weber, A. E. Senior, *Journal of Biological Chemistry* **270**, 19383 (Aug 18, 1995).
24. M. K. al-Shawi, A. E. Senior, *Journal of Biological Chemistry* **268**, 4197 (Feb 25, 1993).
25. T. Kwan *et al.*, *Molecular Pharmacology* **58**, 37 (Jul, 2000).
26. T. W. Loo, D. M. Clarke, *Journal of Biological Chemistry* **272**, 31945 (Dec 19, 1997).
27. T. W. Loo, D. M. Clarke, *Journal of Biological Chemistry* **275**, 39272 (Dec 15, 2000).
28. T. W. Loo, D. M. Clarke, *Journal of Biological Chemistry* **276**, 14972 (May 4, 2001).

29. T. W. Loo, M. C. Bartlett, D. M. Clarke, *Journal of Biological Chemistry* **278**, 39706 (Oct 10, 2003).
30. T. W. Loo, M. C. Bartlett, D. M. Clarke, *Biochemical Journal* **399**, 351 (Oct 15, 2006).
31. G. Tombline *et al.*, *Archives of Biochemistry & Biophysics* **445**, 124 (Jan 1, 2006).
32. T. W. Loo, M. C. Bartlett, D. M. Clarke, *Journal of Biological Chemistry* **279**, 7692 (Feb 27, 2004).
33. T. W. Loo, M. C. Bartlett, D. M. Clarke, *Journal of Biological Chemistry* **279**, 18232 (Apr 30, 2004).